

# SIMULTANEOUS EVOLUTION OF THE VIRIAL PARAMETER AND STAR FORMATION RATE IN MOLECULAR CLUMPS UNDERGOING GLOBAL HIERARCHICAL COLLAPSE

VIANEY CAMACHO<sup>1</sup>, ENRIQUE VÁZQUEZ-SEMADENI<sup>1</sup>, AINA PALAU<sup>1</sup>, GEMMA BUSQUET<sup>2,3</sup>, MANUEL ZAMORA-AVILÉS<sup>4</sup>

<sup>1</sup>Instituto de Radioastronomía y Astrofísica, UNAM, Apartado Postal 3-72, 58089 Morelia Michoacán, México

<sup>2</sup>Institut de Cincies de l'Espai (ICE, CSIC), Can Magrans, s/n, 08193 Cerdanyola del Valls, Catalonia, Spain

<sup>3</sup>Institut d'Estudis Espacials de Catalunya (IEEC), 08034 Barcelona, Catalonia, Spain

<sup>4</sup>CONACYT-Instituto Nacional de Astrofísica, Óptica y Electrónica, Luis E. Erro 1, 72840 Tonantzintla, Puebla, México

## ABSTRACT

We compare dense clumps and cores in a numerical simulation of molecular clouds (MCs) undergoing global hierarchical collapse (GHC) to observations in two MCs at different evolutionary stages, the Pipe and the G14.225 clouds, to test the ability of the GHC scenario to follow the early evolution of the energy budget and star formation activity of these structures. In the simulation, we select a region that contains cores of sizes and densities similar to the Pipe cores, and find that it evolves through accretion, developing substructure similar to that of G14.225 cloud after  $\sim 1.6$  Myr. Within this region, we follow the evolution of the Larson ratio  $\mathcal{L} \equiv \sigma_v/R^{1/2}$ , where  $\sigma_v$  is the velocity dispersion and  $R$  is the size, the virial parameter  $\alpha$ , and the star formation activity of the cores/clumps. In the simulation, we find that as the region evolves: *i*) its clumps have  $\mathcal{L}$  and  $\alpha$  values first consistent with those of the Pipe substructures and later with those of G14.225; *ii*) the individual cores first exhibit a decrease in  $\alpha$  followed by an increase when star formation begins; *iii*) collectively, the ensemble of cores/clumps reproduces the observed trend of lower  $\alpha$  for higher-mass objects, and *iv*) the star formation rate and star formation efficiency increase monotonically. We suggest that this evolution is due to the simultaneous loss of externally-driven compressive kinetic energy and increase of the self-gravity-driven motions. We conclude that the GHC scenario provides a realistic description of the evolution of the energy budget of the clouds' substructure at early times, which occurs simultaneously with an evolution of the star formation activity.

*Keywords:* ISM: clouds – ISM: kinematics and dynamics – stars: formation

## 1. INTRODUCTION

One of the most studied parameters of molecular cloud (MC) structure is the so-called *virial parameter*  $\alpha$ , defined as the ratio of twice the kinetic energy,  $E_K$ , to the gravitational energy,  $E_g$ , for a uniform-density sphere (Bertoldi & McKee 1992),

$$\alpha \equiv \frac{2E_K}{|E_g|} = \frac{5\sigma_v^2 R}{GM}, \quad (1)$$

where  $\sigma_v$  is the average one-dimensional velocity dispersion along the line of sight,  $R$  is the characteristic radius of the cloud, and  $M$  its mass.

The standard notion of MCs is that they are quasi-virialized structures, in which their self-gravitational energy is globally balanced by the turbulent energy (e.g., Larson 1981; Mac Low & Klessen 2004; McKee & Ostriker 2007; Ballesteros-Paredes et al. 2007; Heyer et al. 2009)<sup>1</sup>. In this case, the virial parameter of MCs in gen-

eral should be  $\sim 1$ . Observationally, however, the virial parameter of MCs and their substructures (parsec-scale clumps and 0.1-pc scale cores) appears to be significantly larger than unity for clumps of low column density or low mass, and to decrease systematically to values smaller than unity for objects of higher column density, or higher mass (e.g., Kauffmann et al. 2013; Leroy et al. 2015; Liu et al. 2015; Ohashi et al. 2016; Sanhueza et al. 2017; Contreras et al. 2018; Traficante et al. 2018a; Louvet et al. 2018).

The large values of  $\alpha$  (significantly larger than unity) observed in clouds of low column densities or masses are often interpreted in terms of the presence of a large external confining pressure ( $P/k_B \sim 10^4 - 10^6$  K cm<sup>-3</sup>; e.g., Keto & Myers 1986; Oka et al. 2001; Field et al. 2011; Leroy et al. 2015; Traficante et al. 2018a), although it is hard to imagine that such high pressures can be thermal

pears that MCs tend to be generally magnetically supercritical, and thus cannot be globally supported by magnetic fields (e.g., Crutcher 2012)

<sup>1</sup> Magnetic support has recently lost appeal because it now ap-

in general, since the mean ambient thermal pressure in the ISM is rather low,  $\sim 3 - 4 \times 10^3 \text{ K cm}^{-3}$ , and large deviations from it occur very infrequently (e.g., [Boulares & Cox 1990](#); [Jenkins 2004](#); [Jenkins, & Tripp 2011](#)). Instead, it is most likely that these values correspond to ram pressure, in which case they imply mass, momentum and energy flux across Eulerian cloud boundaries, or a displacement of Lagrangian boundaries ([Ballesteros-Paredes et al. 1999](#); [Banerjee et al. 2009](#)). Indeed, in a previous study ([Camacho et al. 2016](#)), we find, through measurement of the mean velocity divergence within the clouds in numerical simulations of cloud formation and evolution, that roughly half the clouds with an excess of kinetic energy are undergoing compression. This can be interpreted as the clouds being subject to a ram pressure (which amounts to an inertial compression) that is making them denser and smaller, so that they eventually will become gravitationally bound. The origin of this ram pressure can be large scale turbulence, a large scale potential well or other instabilities. Furthermore, one important possibility is that clouds may be falling into the potential well of a stellar spiral arm, which is the main source of large-scale compression for the gas in the Galactic disk ([Roberts 1969](#)). Thus, this is not really a “confinement”, since the clouds are not at rest. The same goes for the other half of the clouds, which are undergoing expansion. In this case, the excess of kinetic energy corresponds to the expansion motions, and again the cloud is not confined, so there is no need for a high confining pressure. In [Camacho et al. \(2016\)](#) and [Ballesteros-Paredes et al. \(2018, hereafter BP+18\)](#) it has been suggested that, for clouds formed by inertial compressions in the background medium ([Ballesteros-Paredes et al. 1999](#)), and which gradually become more strongly gravitationally bound, while the inertial compressive motions decay or dissipate, the kinetic energy transits from being dominated by the inertial motions to being dominated by the gravitationally-driven motions (see also [Collins et al. 2012](#)). In that case, an initial decay of the Larson ratio and the virial parameter may be expected.

On the other hand, values of  $\alpha$  smaller than unity have been interpreted as either being in a state of collapse and/or support from strong magnetic fields (e.g., [Kauffmann et al. 2013](#); [Liu et al. 2015](#); [Ohashi et al. 2016](#); [Sanhueza et al. 2017](#); [Contreras et al. 2018](#)). However, BP+18 recently proposed that values of  $\alpha < 1$  may be expected in cores that have just recently decoupled<sup>2</sup> from the general cloud flow and begun to collapse lo-

cally if the initial inertial motions are also smaller than the virial value. This can be seen by assuming that the non-thermal contribution to the velocity dispersion,  $\sigma_{\text{nth}}$ , consists itself of two contributions, one being a gravitationally-driven infall velocity  $\sigma_{\text{g}}$ , and the other a truly turbulent (or inertial; i.e., not consisting of infall motions) one dimensional component<sup>3</sup>,  $\sigma_{\text{t}}$ , so that

$$\sigma_{\text{nth}}^2 = \sigma_{\text{g}}^2 + \sigma_{\text{t}}^2. \quad (2)$$

Next, BP+18 pointed out that, when a core of fixed mass  $M$  begins to contract locally, it does so from a finite radius  $R_0$ . Thus, its gravitationally-driven velocity  $\sigma_{\text{g}}$  at a later, smaller radius  $R$ , is given by the condition  $E_{\text{K}} + E_{\text{g}} = E_{\text{tot}}$ , where

$$E_{\text{K}} = \frac{1}{2} M \sigma_{\text{g}}^2 \quad (3)$$

and

$$E_{\text{g}} = -\eta \frac{GM^2}{R}, \quad E_{\text{tot}} = -\eta \frac{GM^2}{R_0}, \quad (4)$$

where  $\eta$  is a parameter of order unity that depends on the geometry of the cloud. Thus,

$$\sigma_{\text{g}} = \sqrt{2\eta GM \left( \frac{1}{R} - \frac{1}{R_0} \right)}. \quad (5)$$

As a consequence, the contribution of  $\sigma_{\text{g}}$  to the so-called *Larson ratio*,

$$\mathcal{L} \equiv \frac{\sigma_{\text{v}}}{R^{1/2}} \quad (6)$$

in this fixed-mass core scales with column density as

$$\mathcal{L}_{\text{g}} = \sqrt{2\pi\eta G\Sigma \left[ 1 - \left( \frac{\Sigma_0}{\Sigma} \right)^{1/2} \right]}, \quad (7)$$

while its contribution to the virial parameter scales as

$$\alpha_{\text{g}} = 2 \left[ 1 - \left( \frac{\Sigma_0}{\Sigma} \right)^{1/2} \right], \quad (8)$$

where  $\Sigma_0$  is the column density of the core when it began its contraction.

On the other hand, simultaneously with the variation of  $\sigma_{\text{g}}$  with column density as the core collapses, BP+18 assumed that the inertial contribution to the Larson ratio and the virial parameter decreases by dissipation during the compression at two different plausible rates. Thus, the total value of  $\mathcal{L}$ , obtained in quadrature from the gravitational and the inertial contributions, may adopt

<sup>3</sup> Note that this assumption differs from the very common one that the non-thermal component of  $\sigma$  is due exclusively to the turbulent motions. However, under the assumption in GHC that there are infall motions at all scales in the cloud, it becomes necessary to distinguish the turbulent and the infall contributions to the non-thermal velocity dispersion.

<sup>2</sup> As explained in [Vázquez-Semadeni et al. \(2019\)](#), in the Global Hierarchical Collapse (GHC) scenario, clouds are collapsing globally and therefore the mean Jeans mass in them decreases with time. As a consequence, turbulent density fluctuations (cores) “decouple” from the general cloud flow and begin to collapse themselves when the average Jeans mass in the cloud becomes smaller than their own mass.

a variety of shapes depending on the initial ratio of the two contributions, as shown in Fig. 1 of BP+18.

Another representation of the total virial parameter can be inferred from eqs. (1) and (2). From this, it follows that  $\alpha_{\text{tot}} = \alpha_{\text{t}} + \alpha_{\text{g}}$ . Thus, according to Eq. (5), the virial parameter is

$$\alpha = \frac{3\sigma_{\text{t}}^2 R}{\eta GM} + 2 \left( 1 - \frac{R}{R_0} \right). \quad (9)$$

In this equation the first term can be recognized as the common definition of the virial parameter, while the second term represents the gravitational contribution that depends on size.

It is important to note that, in the above treatment, a Lagrangian definition of the core was used, so that, by construction, the core has a constant mass, and thus this simple calculation cannot predict a dependence of the virial parameter with mass. However, if the core is instead defined in terms of a density or column-density threshold, as is standard for cores defined in terms of molecular-line tracers and common in numerical simulations (e.g., Vázquez-Semadeni et al. 1997; Ballesteros-Paredes & Mac Low 2002; Galván-Madrid et al. 2007; Naranjo-Romero et al. 2015; Camacho et al. 2016; Ibáñez-Mejía et al. 2016), then the mass of a gravitationally contracting core increases with time together with its column density (Naranjo-Romero et al. 2015). Thus, we expect the virial parameter of populations of cores defined by molecular-line tracers to depend on mass as well.

It is important to remark that this kind of evolution occurs in the scenario of Global Hierarchical Collapse (GHC), in which cores begin to collapse locally within a larger cloud that is itself Jeans unstable as well, so that the evolution consists of a multi-scale, hierarchically nested, sequence of collapses (Vázquez-Semadeni et al. 2009; Naranjo-Romero et al. 2015; Vázquez-Semadeni et al. 2017, 2019). This is important in order to allow accretion from the clump onto the core (Naranjo-Romero et al. 2015). In this scenario, the star formation rate (SFR) of the clouds and their substructure also increases as the cloud globally contracts, until the feedback from massive stars, which appear late (after  $\sim 5$  Myr) in the evolution of the cloud, begins to destroy it, either by dispersing or evaporating the dense gas. At this point, the cloud's SFR begins to decrease again (Zamora-Avilés et al. 2012; Zamora-Avilés & Vázquez-Semadeni 2014; Lee et al. 2016; Vázquez-Semadeni et al. 2017, 2018; Caldwell & Chang 2018).

Ballesteros-Paredes et al. (2018) showed that, in isothermal numerical simulations of driven turbulence at the parsec scale, the Larson ratio of cores evolves in the  $\mathcal{L}$  vs.  $\Sigma$  diagram. In the present paper, we show this evolution, as well as that of the virial parameter, in a

larger-scale, multi-phase simulation (of size 256 pc) of giant molecular cloud formation and its subsequent gravitational contraction, and show that it occurs simultaneously with an evolution of the star formation activity of the cores. With the aim to test the GHC hypothesis that the kinetic energy in the cloud and its substructures is dominated by self-gravity, we do not include stellar feedback in the simulation. We also search for the signature of this simultaneous evolution of the virial parameter and the SFR in observational data by comparing the location of the simulated cores and those in star-forming regions of presumably different evolutionary stages, in  $\mathcal{L}$  vs.  $\Sigma$  and  $\alpha$  vs.  $M$  diagrams, and show that there is good qualitative agreement, thus supporting the evolutionary nature of the GHC scenario for molecular clouds.

The plan of the paper is as follows. In Section 2 we briefly describe the simulation and the data from the literature. Next, Section 3 presents the procedure to derive the physical parameters for both the numerical and the observational data. The results about the evolution and the energy budget for both samples are reported in Section 4. Finally, we discuss our findings in Section 5 and a brief summary in Section 6.

## 2. DATA

### 2.1. Observational data

As described in Sec. 1, in order to search for evolutionary effects in clouds, we selected two star-forming regions likely to be in different evolutionary stages. According to the model of Zamora-Avilés & Vázquez-Semadeni (2014, see also Vázquez-Semadeni et al. 2018), this evolution should manifest itself in different values of the cloud's star formation rate and efficiency. Thus, we consider the Pipe Nebula (Alves et al. 2007; Rathborne et al. 2008; Lada et al. 2008), a quiescent dark cloud, and G14.225-0.506 (Busquet et al. 2013; Lin et al. 2017), an infrared dark cloud (IRDC) showing active star formation (Povich et al. 2016).

The Pipe Nebula has been studied in both dust extinction (e.g., Lombardi et al. 2006; Alves et al. 2007; Román-Zúñiga et al. 2010; Ascenso et al. 2013) and molecular line emission ( $\text{C}^{18}\text{O}$ ,  $\text{NH}_3$ ,  $\text{CCS}$ ,  $\text{HC}_5\text{N}$ ; e.g., Muench et al. 2007; Rathborne et al. 2008; Frau et al. 2010, 2012). It is located at a distance of  $\sim 145$  pc (Alves & Franco 2007), and has a mass  $\sim 8000 M_{\odot}$  defined out to an extinction  $A_{\text{V}} = 0.1$  mag (Lada et al. 2010) and a size  $\sim 3 \times 14$  pc (Lada et al. 2008). A large population of dense cores has been identified in this cloud with masses  $0.2\text{--}20 M_{\odot}$  (Rathborne et al. 2008; Frau et al. 2012). We selected the sample of the cores with  $\text{NH}_3$  emission.

IRDC G14.225-0.506 (hereafter G14 for short; Busquet et al. 2013), is part of a large molecular cloud which is actively forming stars (Povich & Whitney 2010; Busquet

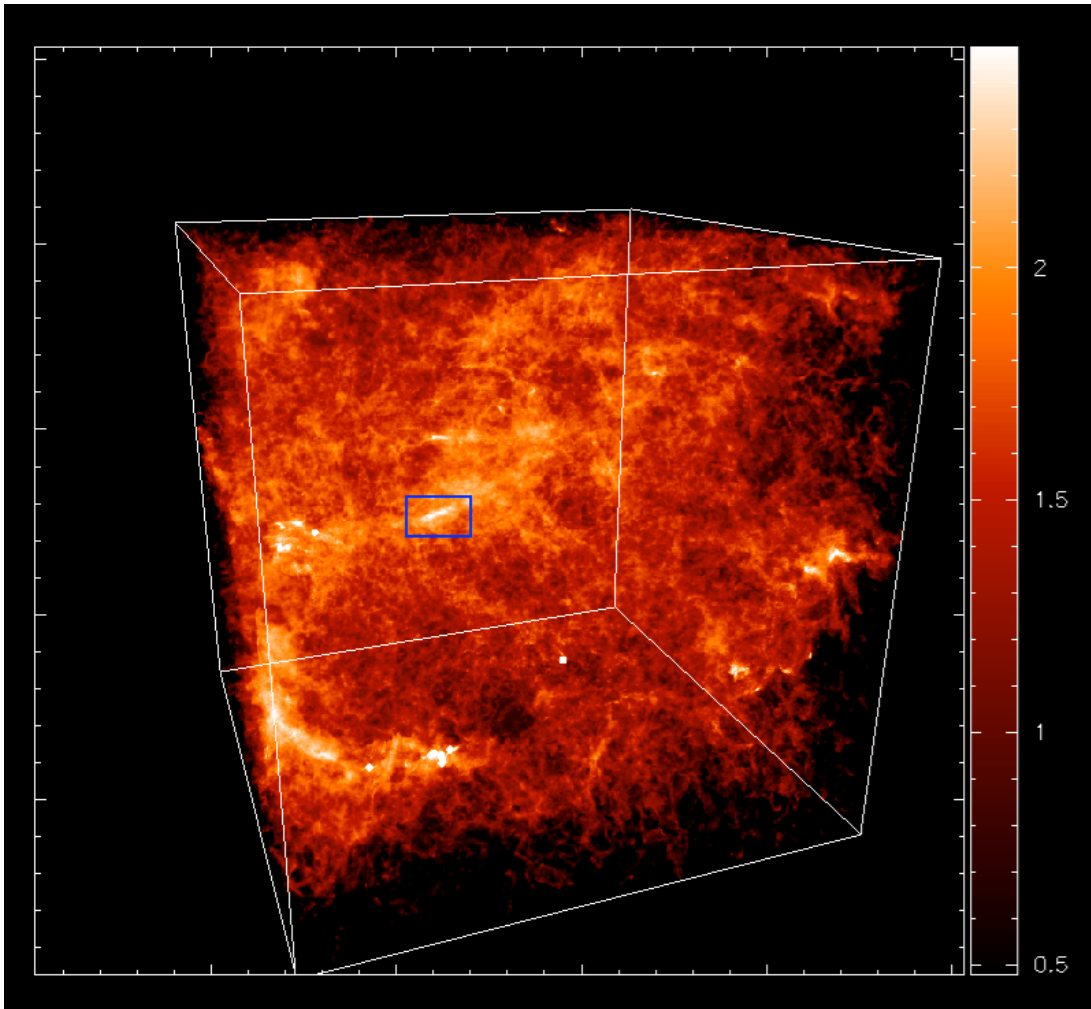


**Figure 1.** The simulation after 20.45 Myr of evolution. The box spans 256 pc on a side, and contains a total mass  $1.5 \sim 10^6 M_{\odot}$ . The blue rectangle shows the region studied in this paper, hereafter referred to as Region A. The white dots represent sink particles, which are still scarce at the time shown. The color bar indicates the column density in internal code units.

et al. 2016; Chen et al. 2019; Shimoikura et al. 2019, and references therein). G14 has a mass  $\sim 1.9 \times 10^4 M_{\odot}$  (Lin et al. 2017), size  $\sim 4.7 \times 8.7$  pc (Busquet et al. 2013), and is located at a distance  $\sim 1.98$  kpc (Xu et al. 2011). In Busquet et al. (2013, hereafter B+13), a study of this cloud was presented in the  $\text{NH}_3$  (1,1) and (2,2) lines, resulting from a combination of Very Large Array (VLA) and Effelsberg 100 m telescope observations. We refer the reader to B+13 for details on the observations and data reduction. In addition, for consistency with the available data from the Pipe Nebula, the FIR/submm-derived column density map towards the G14 cloud was also considered (Lin et al. 2017). The dust emission map is the result from a combination of ground-based and space telescope observations resulting in an angular resolution  $\sim 10''$ , which is comparable to the resulting synthesized beam of  $\text{NH}_3$  in B+13,  $\sim 8'' \times 7''$ .

We assumed that these two clouds represent different

stages of molecular cloud evolution, due to their different levels of star formation activity, as proposed in Vázquez-Semadeni et al. (2018), so that they can be compared to different temporal snapshots of the simulation (Sec. 4.2).

## 2.2. Numerical simulation

In order to test the GHC scenario, we choose a numerical simulation in which the clouds are born as a consequence of turbulence in the diffuse atomic medium, and then engage in global hierarchical collapse as they become dominated by self gravity. This simulation, hereafter RUN03, has been studied in previous works (Heiner et al. 2015; Camacho et al. 2016) and was performed with the GADGET-2 code (Springel 2005) in a box of 256 pc per side containing  $296^3 \approx 2.6 \times 10^7$  SPH particles. Figure 1 shows the whole computational domain of the simulation, 20.45 Myr after the start of the simulation, and just before the first timestep considered in our analysis

Pipe sample							
ID <sup>a</sup>	R <sup>b</sup> (pc)	M <sup>a,b</sup> ( $M_{\odot}$ )	$\sigma_{v,1D}^{a,c}$ ( $\text{km s}^{-1}$ )	ID <sup>a</sup>	R <sup>b</sup> (pc)	M <sup>a,b</sup> ( $M_{\odot}$ )	$\sigma_{v,1D}^{a,c}$ ( $\text{km s}^{-1}$ )
6	0.12	3.14	0.09	65	0.06	0.72	0.26
7	0.14	4.69	0.08	70	0.08	1.14	0.23
8	0.12	3.26	0.11	87	0.17	10.3	0.14
12	0.23	20.3	0.15	89	0.09	1.36	0.10
14	0.17	9.73	0.14	91	0.07	1.09	0.07
15	0.12	2.64	0.18	92	0.09	1.61	0.19
17	0.07	0.69	0.25	93	0.12	3.55	0.17
20	0.11	2.28	0.17	97	0.18	5.86	0.21
22	0.08	1.01	0.12	101	0.08	1.87	0.09
23	0.16	1.87	0.07	102	0.19	6.71	0.24
25	0.09	1.10	0.20	108	0.08	0.78	0.16
40	0.19	9.23	0.10	109	0.12	3.63	0.08
41	0.08	1.08	0.12	113	0.10	2.39	0.06
42	0.09	2.79	0.11	132	0.15	4.67	0.18
47	0.09	1.41	0.14				

**Table 1.** Physical properties for the selected sample of the Pipe cores. a) Rathborne et al. (2008), b) Lada et al. (2008) c)  $\sigma_{v,1D}$  from the  $\text{NH}_3(1,1)$  emission.

below. The blue rectangle shows the region where our numerical cloud is located, illustrating how it fits in the global context of the turbulent ISM in the simulation. At this time, star formation is still mild throughout the simulation, and has not started yet in the region under consideration.

The simulation was initialized with a turbulent driver during the first 0.65 Myr applied at scales from 1 to 1/4 of the numerical box size, reaching a peak velocity dispersion  $\sim 18 \text{ km s}^{-1}$  at that time, after which the simulation was left to decay. It also includes a prescription for the formation of sink particles (see Heiner et al. 2015, for details), and the fix by Abel (2011) that eliminates several unphysical effects of the SPH scheme. These initial conditions result in a clumpy medium that evolves self-consistently from long before the clouds become massive enough to be considered molecular. During this evolution, the clouds grow in mass, size and density by accretion from the diffuse environment, driven first by the inertial flow from the turbulence, and later by their self-gravity. The clouds in the simulation begin to globally contract gravitationally at  $t \sim 10$  Myr after the start of the simulation, and sink particles start forming at  $t \sim 16$  Myr. This simulation was evolved for a total of  $\approx 34$  Myr.

### 3. METHODOLOGY

In order to meaningfully compare the numerical and the observational data, we need to carefully select the region to be studied in the simulation and, for the observations, to ensure consistency between the two datasets. In the simulation, we choose to study a single star-forming region at various times in order to determine its energy

budget evolution. The region was studied using various density thresholds to define its internal structure, in order to explore objects from the scale of molecular clouds to that of dense cores. For the observational data, in the case of the Pipe, we consider a core sample previously identified in the literature (see description below), while for G14 we create our own sample of filaments, clumps and cores directly from the maps.

#### 3.1. The Pipe sample

The Pipe Nebula has more than a hundred identified dense cores (Lada et al. 2008). Because line emission measurements provide the kinematic information, in this work we selected those cores that have been detected in  $\text{NH}_3$  (Rathborne et al. 2008), from which the velocity dispersion is obtained. The mass of these cores is reported in Lada et al. (2008), and spans a range of  $\sim 0.5\text{--}20 M_{\odot}$ . These masses have been determined from the extinction maps, as is the size, which has been computed assuming spherical geometry given the area in the plane of the sky, so that  $R = (A/\pi)^{1/2}$  (Lada et al. 2008). The range in size for the selected cores is  $\sim 0.06\text{--}0.3$  pc and the mean density of the cores is  $\sim 7 \times 10^3 \text{ cm}^{-3}$  (see Table 2 of Rathborne et al. 2008). We use the data reported in these works for our analysis. Table 1 shows the data for the selected sample and Fig. 3 shows the correspondent mass-size relation.

#### 3.2. The G14 sample

In the case of G14 data, we created a clump ensemble by identifying the structures with the `dendrogram`<sup>4</sup> al-

<sup>4</sup> This research made use of `AstroDendro`, a Python package to compute dendrograms of Astronomical data (<https://github.com>).

G14 sample							
ID <sup>a</sup>	R <sup>b</sup> (pc)	M <sup>c</sup> (M <sub>⊙</sub> )	σ <sub>v,1D</sub> <sup>d</sup> (km s <sup>-1</sup> )	ID <sup>a</sup>	R <sup>b</sup> (pc)	M <sup>c</sup> (M <sub>⊙</sub> )	σ <sub>v,1D</sub> <sup>d</sup> (km s <sup>-1</sup> )
C1	0.079	8.519	0.437	C11	0.191	214.234	0.955
C2	0.084	7.828	0.471	C12	0.124	47.156	0.556
C3	0.109	22.760	0.522	C13	0.213	204.163	0.972
C4	0.107	20.686	0.803	c <sub>o</sub> 1	0.092	80.153	0.892
C5	0.054	6.169	0.773	c <sub>o</sub> 2	0.099	66.107	0.981
C6	0.056	6.494	0.573	f1	0.511	636.414	1.096
C7	0.096	21.406	0.544	f2	0.488	648.723	0.811
C8	0.057	6.741	0.437	f3	0.274	98.919	0.582
C9	0.056	8.163	0.561	f4	0.509	574.053	1.333
C10	0.060	8.784	0.790				

**Table 2.** Physical properties for the G14 sample. a) The IDs in this table correspond to the labeled objects in Fig. (2). b) The size was computed from the area  $A$  defined with the `dendrogram` package,  $R = (A/\pi)^{1/2}$ . c) Mass is computed as  $M = 2.8 m_{\text{H}} N(\text{H}_2) A$ , considering the  $N(\text{H}_2)$  map from Lin et al. (2017) and the hydrogen mass  $m_{\text{H}} = 1.6 \times 10^{-24}$  g. d)  $\sigma_{v,1D}$  was obtained from the  $\text{NH}_3(1,1)$  hyperfine fits.

gorithm (Rosolowsky et al. 2008; Goodman et al. 2009) applied to the moment-0 map of the  $\text{NH}_3$  data. In B+13, two classes of objects, filaments and hubs, were recognized. The former were identified in the  $\text{NH}_3(1,1)$  map, while the latter were identified in the  $\text{NH}_3(2,2)$  map, and correspond to the sites where filaments converge. This indicates that the hubs have larger typical densities than the filaments. It is noteworthy however, that the structures they call “hubs” actually still exhibit elongated morphologies.

We make use of the `dendrogram` algorithm in the ammonia data to define the boundaries of the dense structures similar to those reported in B+13. However, we defined three classes of objects: filaments, clumps and dense cores<sup>5</sup>. Our filaments roughly coincide with those defined in B+13; our clumps include two classes of objects: the hubs from B+13 as well as some isolated roundish clumps away from the filaments. Finally, our dense cores correspond to the densest, roundish regions within B+13’s hubs. According to this classification, we chose different sets of values of the input parameters in the `dendrogram` algorithm, applied to the moment-0 map, to obtain the set of pixels defining each structure. The rms noise of the  $\text{NH}_3$  cube in G14 is 8 mJy/beam per 0.6 km s<sup>-1</sup> spectral channel. B+13 defined the lowest contour level at 3 times the rms noise; thus, we set the noise parameter in the `dendrogram` algorithm to  $\sigma = 3\text{rms}$ . The equivalent area of the beam is  $\sim 12$  pixels ( $\sim 0.1$  pc). Then, we consider a minimum number of pixels of `min_pix` = 15, in order to have structures larger or equal to the beam. Finally, we vary the input parameters by means of `min_value` =  $n_v\sigma$  and `min_delta` =  $n_d\sigma$ . Where  $(n_v, n_d) = (1, 1)$  for the filaments, (5, 1) for the clumps,

com/dendrograms/astrodendro)

<sup>5</sup> We refrain from using the name “hub” for the structures in the simulation in order to avoid confusion.

and (15, 3) for the dense cores.

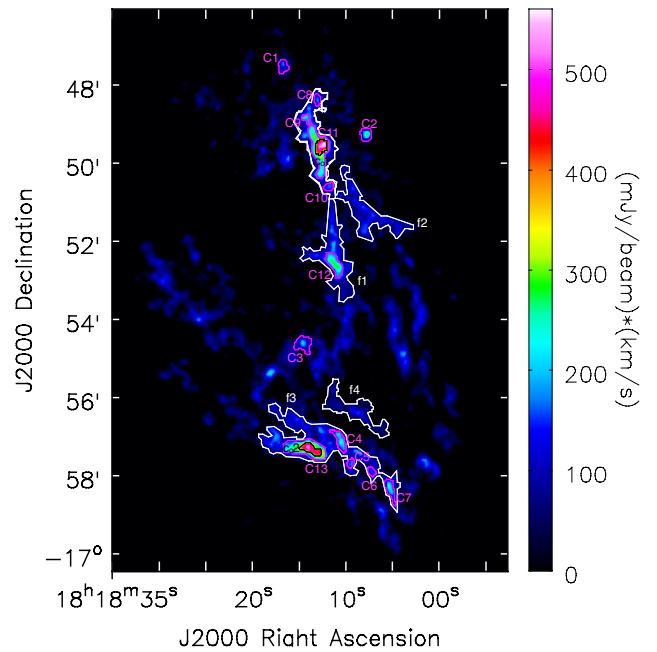


**Figure 2.** G14 moment-0 map of the  $\text{NH}_3(1,1)$  inversion transition taken from Busquet et al. (2013). Contours show the objects of study in this work, the different colors denote the filaments-f (white), clumps-C (magenta) and dense cores-c<sub>o</sub> (black). They have been obtained using the `dendrogram` package.

Figure 2 shows the three main families that have been selected, the filaments (white) labeled with an “f”, the clumps (magenta) labeled with a “C”, and the dense cores (black) labeled with a “c<sub>o</sub>”. In order to investi-

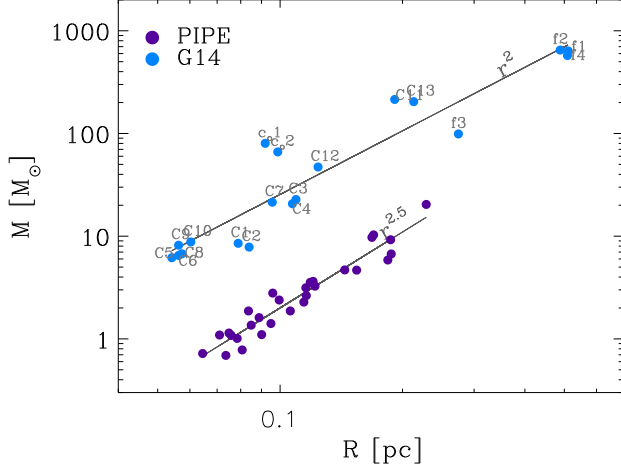


**Figure 3.** Size-mass relation for the selected sample of the Pipe cloud (purple) and the G14 cloud (blue). The objects in the G14 sample correspond to the contours in Fig. 2. We additionally show the corresponding fits,  $r^p$ , for each sample, with  $p \sim 2.5$  for the Pipe and  $p \sim 2$  for the G14 clouds.

gate how the physical properties of the sample change when the `dendrogram` input parameters are modified, Appendix A shows a new sample obtained varying the `min_delta` value.

With the area defined by the set of pixels for each structure, we computed their size. We used the CASA<sup>6</sup> (McMullin et al. 2007) software to extract the spectra in the position-position-velocity cubes for the (1,1) and (2,2)  $\text{NH}_3$  transitions to the contours defined with the dendrograms. For these objects, the one-dimensional velocity dispersion was directly computed as  $\sigma_v = \text{FWHM}/2\sqrt{2\ln 2}$ , where FWHM is the full width at half maximum obtained from the fit to the hyperfine structure of ammonia, performed with the “ $\text{NH}_3(1,1)$ ” CLASS method within the GILDAS<sup>7</sup> software. Table 2 shows the properties derived for the sample in G14. For this case we obtain objects in a size range of 0.05-0.5 pc and mean density  $\sim 2 \times 10^4 \text{ cm}^{-3}$  (see Fig. 4).

Note that, in principle, we could derive the mass of the clumps in G14 directly from the line data for the (1,1) and (2,2)  $\text{NH}_3$  transitions, assuming a certain ammonia abundance. However, for consistency with the Pipe core sample, whose mass estimate was derived with the dust extinction map, we considered the column density map from Lin et al. (2017) to compute the masses within the contours defined in the ammonia maps with the `dendrogram` algorithm, as described above, assuming that the two sets of observations trace the same gas.

<sup>6</sup> <https://casa.nrao.edu/>

<sup>7</sup> <http://www.iram.fr/IRAMFR/GILDAS>

We show in Appendix B a comparison deriving the mass from the ammonia data. Figure 3 shows the mass and size of the objects selected in both the Pipe and G14 clouds. On the other hand, Fig. 4 shows the density histogram for both clouds. We can observe that the Pipe cloud sample contains cores with similar densities, while the G14 sample covers a larger density range, varying from filaments to dense cores.

In this way, for both clouds we have the mass derived from dust emission and the velocity dispersion derived from the  $\text{NH}_3$  emission. Using the values of  $M$ ,  $R$ , and  $\sigma_v$  thus derived, we compute the virial parameter (eq. 1) and Larson ratio (eq. 6) for the G14 clumps and cores that will be discussed in section 4. For the Pipe cores, we use the  $M$ ,  $R$ , and  $\sigma_v$  reported in the literature (Table 1).

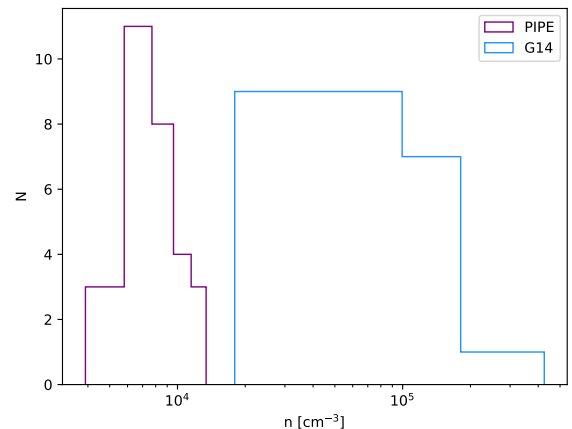


**Figure 4.** Density histograms for the selected sample of the Pipe cloud (purple) and the G14 cloud (blue).

### 3.3. The numerical sample

In the simulation, several star forming regions are formed from the collapse of the density fluctuations present in the clouds. As the parent cloud collapses, its mean Jeans mass decreases. Then, dense turbulent fluctuations collapse once they exceed their Jeans mass and quickly start forming stellar particles (Girichidis et al. 2014; Zamora-Avilés & Vázquez-Semadeni 2014; Vázquez-Semadeni et al. 2019). Thus, most of them reach a high star formation activity in a short time. At these stages, feedback should have important effects, affecting the kinematics around the clumps and reducing the SFR if it were included. However, it is not considered in the simulation. Thus, to avoid objects that should already be affected by feedback, possibly in the process of dispersal, we search for a star forming region in an intermediate time interval in the simulation ( $\approx 18 - 23 \text{ Myr}$ )

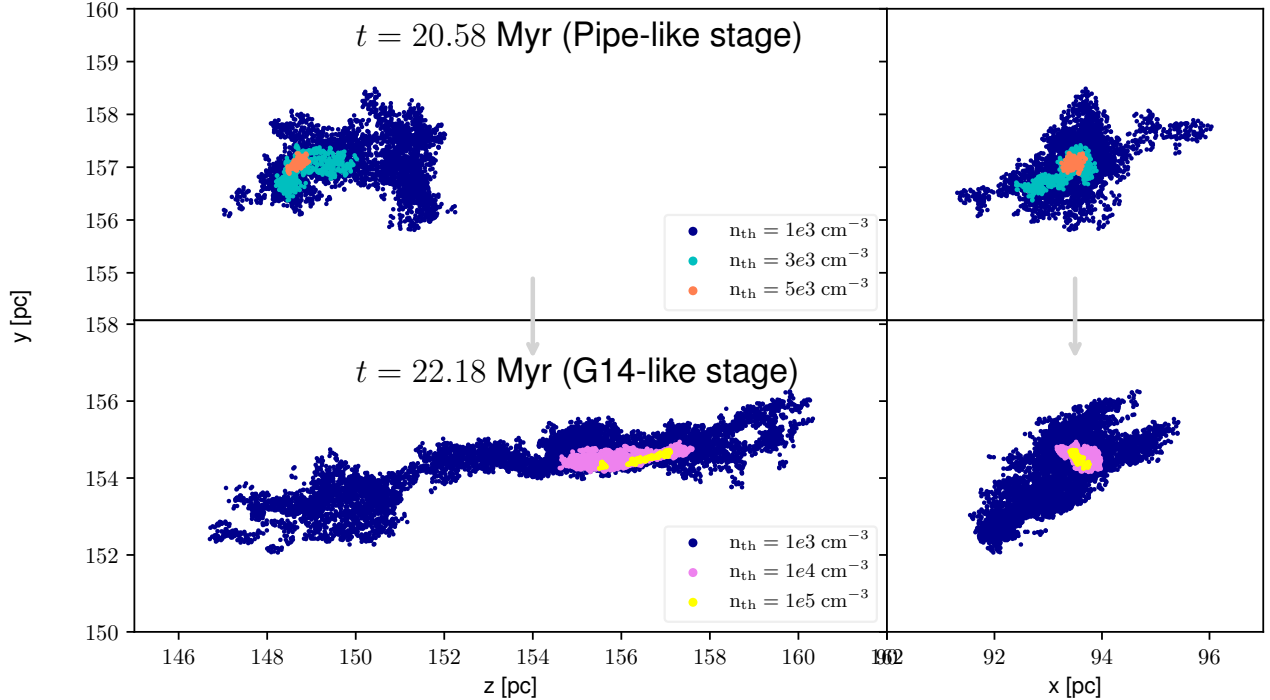


**Figure 5.** Numerical clump at the initial and final times in two different planes and at different density thresholds. The top panels show the numerical clump at  $t = 20.58$  Myr, the time when we define the Pipe-like core (orange,  $n_{th} = 5 \times 10^3 \text{ cm}^{-3}$ ). At this stage the clump can be compared to the substructure in the Pipe. The bottom panels show the numerical clump at an advanced stage,  $t = 22.18$  Myr. At this time, the cloud can be compared with the filamentary structure in G14.

such that the simulation has dissipated enough kinetic energy from the initial turbulent fluctuations in order to have realistic velocity dispersion values, and does not yet have too high a star formation activity at late stages, such that stellar feedback has not had time to affect the region (see Appendix C).

To define different categories of objects like filamentary clumps, hubs and dense cores, we consider density thresholds similar to the mean densities of the corresponding objects in the Pipe and the G14 clouds by applying the clump-finding algorithm for SPH particles described in Camacho et al. (2016)<sup>8</sup>.

Furthermore, for the object selection in the available period, we look for a cloud that meets the following conditions: *a)* to be a single coherent object in the 3D space and not just a random superposition in projection and to remain so over a few million years; *b)* to show a not too

<sup>8</sup> The clump-finding algorithm (see Camacho et al. 2016) works by defining connected regions above a certain density threshold,  $n_{th}$ , in the density field. First,  $n_{th}$  is set, and then the algorithm searches for the particle with the highest density above the threshold and searches for all the neighboring particles around it with densities larger than  $n_{th}$ . In order to have enough mass resolution we considered a minimum of 80 SPH particles in each clump. This algorithm has been designed for working directly on the SPH data and works similarly to the dendrograms algorithm used for the observations, except that it doesn't automatically track the lineage of the substructures.

high star formation efficiency, for the entire cloud we tolerate a SFE  $\sim 20\%$ ; *c)* not to be located near the edges of the box to allow a straightforward identification of the objects without cross boundary complications. The requirements mentioned here restrict the number of objects that can be analyzed. Moreover, the cores evolve rapidly in comparison to the time interval between snapshots,  $\Delta t = 0.133$  Myr. Therefore, the cores become larger, denser and more massive within a few snapshots.

We selected from the simulation a clump that fulfills the above criteria. We refer to it simply as “the numerical clump”. This clump was followed over a timespan  $\sim 1.6$  Myr, from 20.58 to 22.18 Myr, in a region of  $7 \times 8 \times 19$  pc in which the clump evolves. In what follows, we refer to this region as “Region A” (Fig. 1). The initial time was selected as the time when cores above a threshold  $n_{th} = 5 \times 10^3 \text{ cm}^{-3}$  first appear in this region.<sup>9</sup> During the above timespan, the clump evolves from being similar to the substructure in the Pipe to being similar to the substructure in G14, and changes in shape, size, mass, and mean and maximum density (Figs. 5-6). Note that, somewhat counterintuitively, the clump *grows* in mass and size during the process, due to the accretion

<sup>9</sup> We use the mean density of the Pipe cores ( $\sim 7 \times 10^3 \text{ cm}^{-3}$ ) as the reference to set the lowest density thresholds.

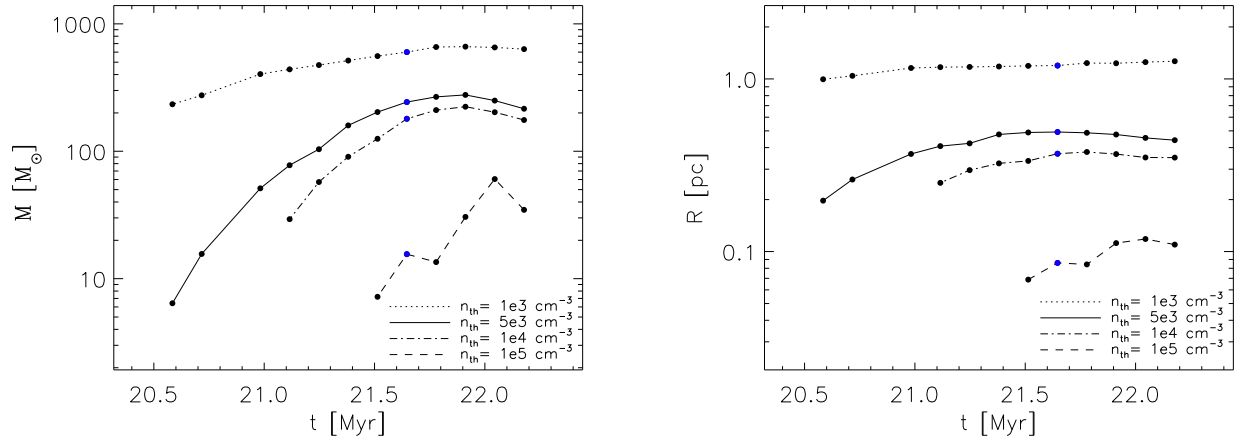


**Figure 6.** Time evolution of the mass and size for the numerical clump. The blue dot corresponds to the time when star formation begins, while different lines correspond to the density thresholds  $n_{\text{th}}$  used to define substructures within the numerical clump.

of external material.

For the Pipe-like stage of the numerical clump, we recall that the Pipe cloud has dimensions  $\sim 3 \text{ pc} \times 14 \text{ pc}$ , and that the more massive cores have masses from  $\sim 5 - 20 M_{\odot}$ , sizes of  $\sim 0.2 \text{ pc}$ , and densities of  $\sim 7 \times 10^3 \text{ cm}^{-3}$ . We thus define the numerical clump by a threshold  $n_{\text{th}} = 10^3 \text{ cm}^{-3}$  and a Pipe-like core at  $n_{\text{th}} = 5 \times 10^3 \text{ cm}^{-3}$ . With these thresholds, the numerical clump has projected dimensions of  $\sim 3 \times 5 \text{ pc}$ , and contains one roundish core of size  $\sim 0.2 \text{ pc}$ , mass  $6.3 M_{\odot}$ , and mean density  $\sim 6330 \text{ cm}^{-3}$ , in good agreement with a typical Pipe core. In order for this object to have dimensions comparable to those of the Pipe cloud, we need to go down to a threshold of  $n_{\text{th}} = 300 \text{ cm}^{-3}$ , for which the resulting numerical cloud has dimensions  $\sim 7 \text{ pc} \times 10 \text{ pc} \times 15 \text{ pc}$ , and mass  $\sim 1100 M_{\odot}$ . This mass is still  $\sim 8$  times lower than the Pipe’s mass as reported by [Lada et al. \(2010\)](#), over an extension of  $3 \times 14 \text{ pc}$ . This suggests that the density profile at the Pipe stage is steeper than in the Pipe, perhaps due to the absence of magnetic field in our simulation, which could tend to smooth out the cloud somewhat.

For the G14-like stage, we defined the clump at  $n_{\text{th}} = 10^3 \text{ cm}^{-3}$ , denser regions at  $n_{\text{th}} = 10^4$ , and a dense core at  $n_{\text{th}} = 10^5 \text{ cm}^{-3}$ . As with the Pipe-like stage, we look for the structure in this epoch at  $n_{\text{th}} = 300 \text{ cm}^{-3}$ . The corresponding mass and projected dimensions at this time are  $\sim 1900 M_{\odot}$  and  $\sim 9 \text{ pc} \times 25 \text{ pc}$ . We see that the total mass of the numerical cloud at this threshold is still a factor of  $\sim 10$  times lower than the mass of G14, while being longer and narrower. Thus the apparently steeper density profile of the numerical cloud remains at this stage.

For the structures thus identified, we compute the

mass as  $M = nm_{\text{sph}}$ , where  $n$  is the total number of particles belonging to the clump and  $m_{\text{sph}}$  is the mass of an SPH particle ( $m_{\text{sph}} = 0.06 M_{\odot}$ ); the size as  $R = (3V/4\pi)^{1/3}$ , where  $V$  is the total volume of the particles<sup>10</sup>; the column density as  $\Sigma = M/\pi R^2$ ; the Larson ratio  $\mathcal{L} = \sigma_{v,1D}/R^{1/2}$ ; and the virial parameter. The latter is computed in the standard form as in eq. (1). We also estimated the instantaneous star formation rate as  $\text{SFR} \approx \Delta M_*/2\Delta t$ , where  $\Delta M_*$  is the mass that is transformed into sink particles during the time interval  $2\Delta t$ , and  $\Delta t$  is the time between snapshots. The mass of the sink particles is not constant, since they accrete material from the surroundings as the simulation evolves. Thus,  $\Delta M_*$  includes the mass in new sinks as well as the mass accreted by existing sinks. Finally, the star formation efficiency at any instant in time  $t$  is computed as  $\text{SFE}(t) = M_*(t)/[M_{\text{gas}}(t) + M_*(t)]$ .

## 4. RESULTS

Observations from molecular clouds to dense cores in  $\mathcal{L} - \Sigma$  diagrams have shown objects below or above the energy equipartition, and where the deviations have been explained assuming unbound clouds, external pressure confinement or turbulence regulation ([Heyer et al. 2009](#); [Field et al. 2011](#); [Traficante et al. 2018a](#)). In the present work we offer a different interpretation for the sub-virial cores.

### 4.1. The numerical clump sample

The energy balance in the numerical clump sample is studied in the  $\mathcal{L} - \Sigma$  diagram (top panels of Figs. 7 and 8). The evolution of the virial parameter  $\alpha$  is shown in

<sup>10</sup> The total volume is the sum of the specific volumes of all particles, see [Camacho et al. \(2016\)](#) for details.

the bottom panels. In addition, in these figures the symbols are colored according to the SFE (Fig. 7) and the SFR (Fig. 8). In the  $\mathcal{L} - \Sigma$  diagram, we refer to the line  $\mathcal{L} = \sqrt{G\Sigma}$  as the “virial line”, and to the line  $\mathcal{L} = \sqrt{2G\Sigma}$  as the “free-fall line” (Ballesteros-Paredes et al. 2011). Since these two lines are so close to each other, we collectively refer to both as “the equipartition condition”. Note that they correspond to values of the virial parameter of  $\alpha = 1$  and  $\alpha = 2$ , respectively. We refer to the region above energy equipartition “super-virial” and to the region below, as “sub-virial”.

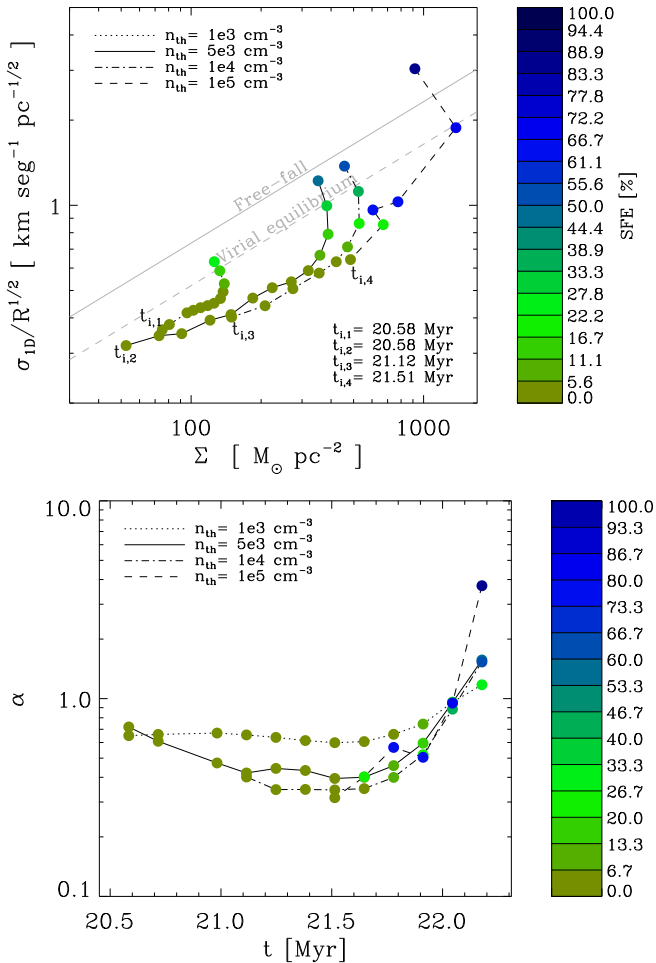


**Figure 7.** Evolution of the substructures in the numerical clump in the  $\mathcal{L} - \Sigma$  diagram (top) and evolution of their virial parameter (bottom). Each point represents a time step in the simulation, the time interval between them is  $\sim 0.13$  Myr. The times when the structures appear for the first time at each threshold are indicated by  $t_{i,n}$ . The final time is 22.18 Myr for structures defined at all density thresholds. Also shown is the evolution of the SFE, indicated by the colorbar.

The various lines correspond to the density thresholds

used to define the substructure in the numerical clump, joining objects defined by the same density threshold. These can be thought of as objects seen in tracers with different critical densities. Thus, the time evolution for an object at a certain density can be seen by following the connected symbols from left to right. We observe in the simulation that denser objects, and eventually stars, appear later in the evolution of the clump. Because of this, we label the beginning of each curve with the time  $t_{i,n}$  when the objects first appear at  $n_{th}$ . In fact, it is

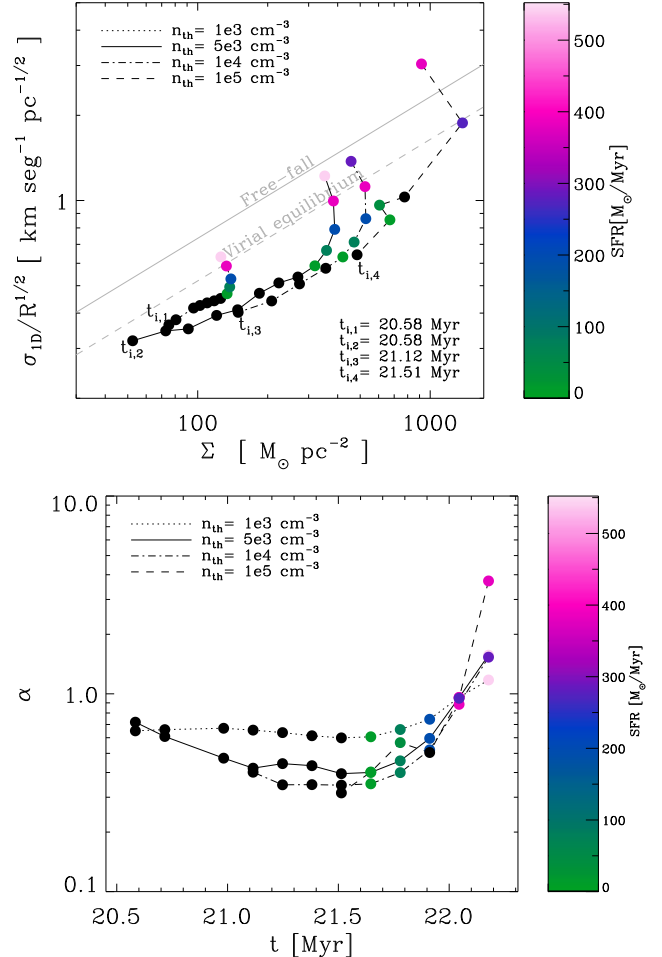


**Figure 8.** Same as Fig. 7 although in these plots the color scheme indicates the SFR.

noteworthy that the first stars appear in the clump approximately one free-fall time of the clump after the time when we first observe it. Indeed, at that time ( $t_0 = 20.58$  Myr), the clump’s mean density is  $\rho = 2.35 \times 10^3$  cm<sup>-3</sup>, for which the free-fall time  $t_{ff} = \sqrt{3\pi/(32G\rho)}$  is  $\approx 0.95$  Myr. On the other hand, the first sink appears 1.06 Myr after  $t_0$ , in very good agreement with the value of  $t_{ff}$ , considering that the actual collapse is always slightly slower because thermal pressure is not totally negligible (Larson 1969). This shows that the clump is evolving essentially

under the action of its own self-gravity.

There are some important features to notice in the  $\mathcal{L} - \Sigma$  diagrams: *i)* the earliest structures appear sub-virial for both low and high densities; *ii)* as the objects evolve in time (see also  $\alpha$  vs.  $t$  plots), they approach equipartition and in one case the object even becomes super-virial. This can be seen for objects defined at all density thresholds.

Additionally, a gradual increase is seen of both the SFR and the SFE, represented by the colors in Figs. 7 and 8. That is, an increase of the SFE and SFR occurs simultaneously with the increase of kinetic energy, manifested in the variation of the Larson ratio and the virial parameter. The increasing star formation activity is a natural consequence for a clump that becomes denser on average due to global gravitational contraction and thus contains a higher fraction of high-density gas (Zamora-Avilés & Vázquez-Semadeni 2014; Vázquez-Semadeni et al. 2018) which is responsible for the ‘instantaneous’ star formation in the clump. Thus, *we suggest that SFR and SFE evolve simultaneously with the energy budget of the clumps.*

It is observed that, early in their evolution, the objects start with low values of  $\alpha$ ; in fact, the clump defined at  $n_{\text{th}} = 10^3 \text{ cm}^{-3}$  remains with  $\alpha$  roughly constant over  $\sim 1$  Myr. For some other clumps, the virial parameter even decreases before star formation begins, to later increase again, approaching the free-fall value ( $\alpha = 2$ ) at times when the SFR has reached values of a few  $\times 100 M_{\odot} \text{ Myr}^{-1}$ . This shows that values of  $1 \lesssim \alpha \lesssim 2$  are not necessarily a signature of unbound objects. Instead, they may be indicative of the approach to the free-fall value.

In addition, Fig. 9 shows the evolution of the numerical clump’s substructure in the  $\alpha$ - $M$  diagram. As in Figs. 7 and 8, the lines connect clumps defined at the same density threshold at different times, indicated by the colorbar. Thus, the set of points shown with a particular color illustrates the hierarchy of nested structures at a given time, while points joined by each line represent the evolution of a clump defined at that threshold. It is noteworthy that the slope of the clump hierarchy at the last time exhibits a negative value. This implies that the most massive objects in a statistical sample, and in a sample including different density thresholds and for later stages, have lower values of  $\alpha$  than the less massive ones, as shown in Fig. 10, in spite of the fact that each structure is seen to evolve from sub-virialization to equipartition, as predicted by eq. (8). This is because, as shown in Vázquez-Semadeni et al. (2019), for a coval sample of cores selected in such a way that their mass scales as  $R^p$ , with  $p < 3$ , as is often the case (see Fig. 3), the more massive objects have lower densities, and therefore longer free-fall times. This implies that, at some age  $t$ , the more massive objects have traversed a

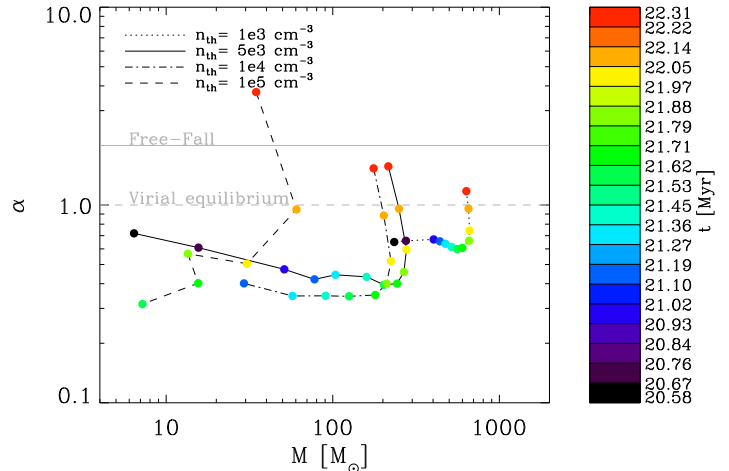


**Figure 9.** Virial parameter  $\alpha$  as a function of mass for the numerical clump and its substructure. The time sequence is shown in colors, while the lines show the density thresholds.

smaller fraction of their free-fall time, and are therefore at earlier stages of their own evolution, therefore being more sub-virial.

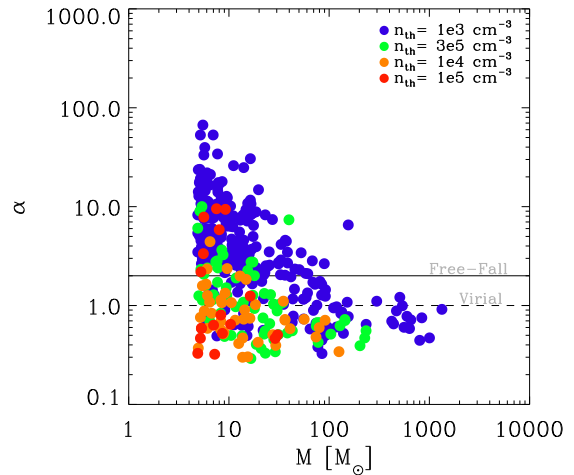


**Figure 10.** Virial parameter for a sample of clumps from the RUN03 simulation. We considered  $t = 20.8, 21.2, 22.2, 24.8$  and  $26.5$  Myr and the same density thresholds for the numerical clump.

#### 4.2. Comparison with the observational sample

As mentioned in Sec. 2, the two real clouds considered in this work are expected to be in different evolutionary stages. Indeed, the Pipe shows little signs of star formation (the component known as B59 or the Mouthpiece is known to have embedded a group of young stars, e.g., Brooke et al. 2007; Román-Zúñiga et al. 2010; Dzib et al. 2013) and a low fraction of its mass at high density

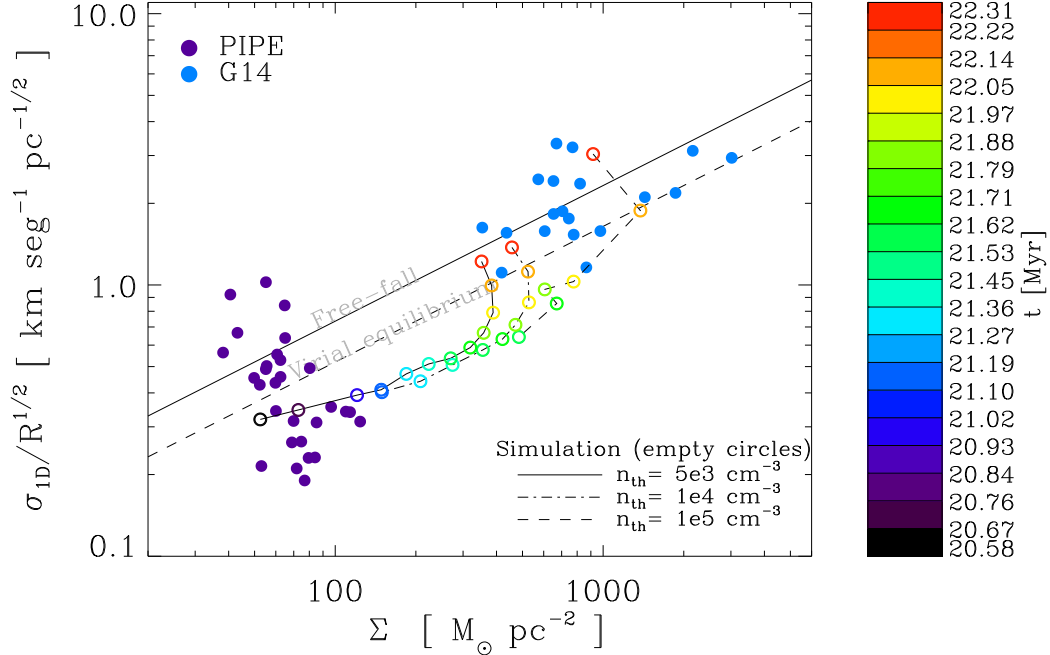


**Figure 11.**  $\mathcal{L} - \Sigma$  diagram for the observational clump sample (purple and blue dots) and comparison with the temporal evolution for some of the substructure in the numerical clump. The simulated clumps (empty circles) evolve from the left to the right, their colors correspond to the color bar in Fig. 9, which represents time.

(Lada et al. 2010), which has been interpreted as an indication of an early evolutionary stage (e.g., Onishi et al. 1999; Rathborne et al. 2008; Lada et al. 2010; Frau et al. 2010, 2015; Vázquez-Semadeni et al. 2018). On the other hand, G14 exhibits active star formation and a duration of the star formation activity of a few Myr, suggestive of a somewhat more advanced evolutionary stage (Povich et al. 2016).

Similarly to what was done for the numerical sample, we plot the corresponding  $\mathcal{L} - \Sigma$  diagram (Fig. 11) and  $\alpha$ -mass plot (Fig. 12) for the substructures in the Pipe (purple dots) and G14 (blue dots) clouds. In Fig. 11, we plot the evolution of the substructures of the numerical clump defined at  $n_{\text{th}} = 5 \times 10^3, 10^4$  and  $10^5 \text{ cm}^{-3}$ , with colors representing the time evolution with the same scheme as in Fig. 9. In particular, the clump at  $5 \times 10^3 \text{ cm}^{-3}$  (black circle) named the “Pipe-like core” (Sec. 3.3), evolves from a locus centered in that of the Pipe cores to one close to the G14 sample. When the Pipe-like core first appears (at 20.58 Myr), it shows a structure similar to the dense cores in the Pipe cloud with,  $M \sim 6.4 M_{\odot}$ ,  $R \sim 0.2 \text{ pc}$  and  $\sigma_{1D} \sim 0.14 \text{ km s}^{-1}$ , and exhibits a low virial parameter  $\sim 0.7$ . As the simulation evolves, the object defined by the same threshold as the Pipe-like core grows in size and mass due to accretion, changing its morphology from roughly spherical to a more elongated structure (its largest axis has  $\sim 3 \text{ pc}$ )<sup>11</sup>. Its mass grows in time

even after the star formation begins (see top panel in Fig. 6). However, after  $\sim 0.3 \text{ Myr}$ , it becomes roughly constant.

At the latest time, the clump defined at  $10^3 \text{ cm}^{-3}$  (Fig. 6), which has a filamentary shape (Fig. 5) can be compared with the filaments f1 and f2 in G14 (see Tab. 2). In the simulation this filamentary clump has mass  $\sim 600 M_{\odot}$  and projected dimensions  $\sim 4 \times 13 \text{ pc}$ , similar to the filaments in G14. On the other hand, the interior regions of the Pipe-like core within higher- $n_{\text{th}}$  thresholds (yellow and red circles in Fig. 11) evolve to positions comparable to those of denser G14 clumps and filaments. At time  $t = 22.04 \text{ Myr}$ , the yellow and red circles at  $n_{\text{th}} = 10^4 \text{ cm}^{-3}$  have  $M \sim 203 M_{\odot}$ ,  $R \sim 0.4 \text{ pc}$ ,  $\sigma_{1D} \sim 0.6 \text{ km s}^{-1}$ , and a virial parameter  $\sim 0.9$ , between f1 and f3 of the G14 sample, while the yellow circle at  $n_{\text{th}} = 10^5 \text{ cm}^{-3}$  has  $M \sim 60 M_{\odot}$ ,  $R \sim 0.1 \text{ pc}$ ,  $\sigma_{1D} \sim 0.6 \text{ km s}^{-1}$ , and a virial parameter  $\sim 0.9$ , in the neighborhood of C11, C12, and C13 (see Tab. 2).

We observe that roughly half of the cores in the Pipe sample (which we consider less evolved; see Sec. 2) appear in the super-virial range in the  $\mathcal{L} - \Sigma$  and the  $\alpha - M$  diagrams. In Camacho et al. (2016) we show that the scatter around equipartition for objects in the low- $\Sigma$  range might be caused either by the dispersion of the

that all particles belonging to a clump are contained in a sphere whose volume is the sum of all the particles’ volumes. Thus, the size,  $R = (3V/4\pi)^{1/3}$ , does not reflect the largest dimension of the clumps.

<sup>11</sup> Recall that the size definition considered in this work assumes

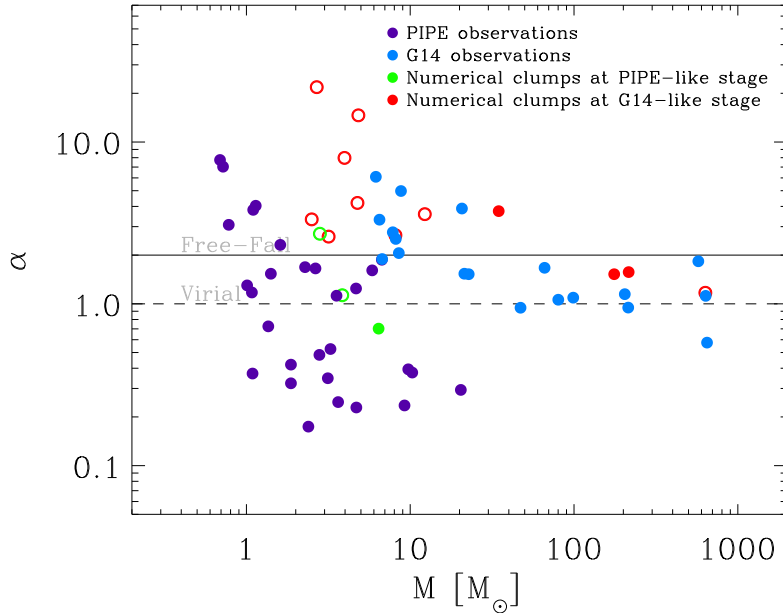


**Figure 12.** Virial parameter for the Pipe (purple dots) and G14 (blue dots) selected clumps. Additionally, other objects in Region A but outside the numerical clump are shown at the Pipe-like stage ( $t = 20.58$  Myr and  $n_{\text{th}} = 5 \times 10^3 \text{ cm}^{-3}$ ) and at the G14-like stage ( $t = 22.18$  Myr), in green and red empty circles respectively. The numerical clump and its substructures are denoted by the filled circles, with green and red again corresponding to the Pipe-like and G14-like stages, respectively.

clumps or by large scale motions assembling them. In the present study, we observe that the super-virial Pipe cores, in Figs. 11 and 12, are the smallest and less massive objects. We suggest that, as discussed in Camacho et al. (2016), in about half the cases, their apparent kinetic energy excess may be a consequence of the externally-driven motions that are assembling them, rather than a signature of being unbound. In the other half, actual dispersal may be occurring, but in no case the objects are confined by large external thermal pressure. On the other hand, the sub-virial cores are in fact the most massive ones, and include some of the cores belonging to the active star forming region B59. As discussed in Ballesteros-Paredes et al. (2018) and Vázquez-Semadeni et al. (2019), their motions may be dominated by their self-gravity, although without having reached the free-fall velocity corresponding to equipartition (cf. eq. (7)). In contrast, the G14 sample (which we consider more evolved) is seen to lack strongly sub-virial objects. This is consistent with the evolution of the numerical sample from sub-virial to super-virial states.

To compare with the numerical sample, in Fig. 12 we show the numerical clump and its substructures, at both the Pipe-like (green filled circles) and the G14-like (red filled circles) stages, 20.58 and 22.18 Myr respectively. Furthermore, we also show other clumps and cores lo-

cated within Region A but outside the numerical clump, shown with green and red empty circles for the Pipe-like and the G14-like stages respectively. Note that in order to include these, we had to reduce our mass resolution criterion to 40 SPH particles, since no additional objects other than the numerical clump with more than 80 SPH particles are found within Region A in this time interval. We can observe that the numerical samples, at their corresponding stages, are consistent with the real clumps, occupying similar loci and exhibiting a negative slope in the  $\alpha$ - $M$  diagram, with the more massive objects having lower  $\alpha$  values.

Concerning the star formation activity, Lada et al. (2010) report an SFR  $\sim 5 M_{\odot} \text{ Myr}^{-1}$  for the Pipe, while Povich et al. (2016) report an SFR  $\sim 7 \times 10^3 M_{\odot} \text{ Myr}^{-1}$  for G14, or roughly 3 orders of magnitude larger than that of the Pipe. Of course, a more meaningful comparison is in terms of the *specific* SFR, or *sfr*, since G14 is clearly a more massive region than the Pipe. Lada et al. (2010) report a total mass for the Pipe of  $\sim 8 \times 10^3 M_{\odot}$ , while Elmegreen et al. (1979) quote a mass  $\sim 2 \times 10^5 M_{\odot}$  for M17 S Wex (see also, Povich et al. 2016; Lin et al. 2017), the parent cloud of the G14 IRDC. Thus, *sfr*  $\sim 6.2 \times 10^{-4} \text{ Myr}^{-1}$  for the Pipe, while *sfr*  $\sim 3.5 \times 10^{-2} \text{ Myr}^{-1}$ . Thus, the specific SFR of G14.2 is  $\sim 50\times$  larger than that of the Pipe, implying indeed a much stronger

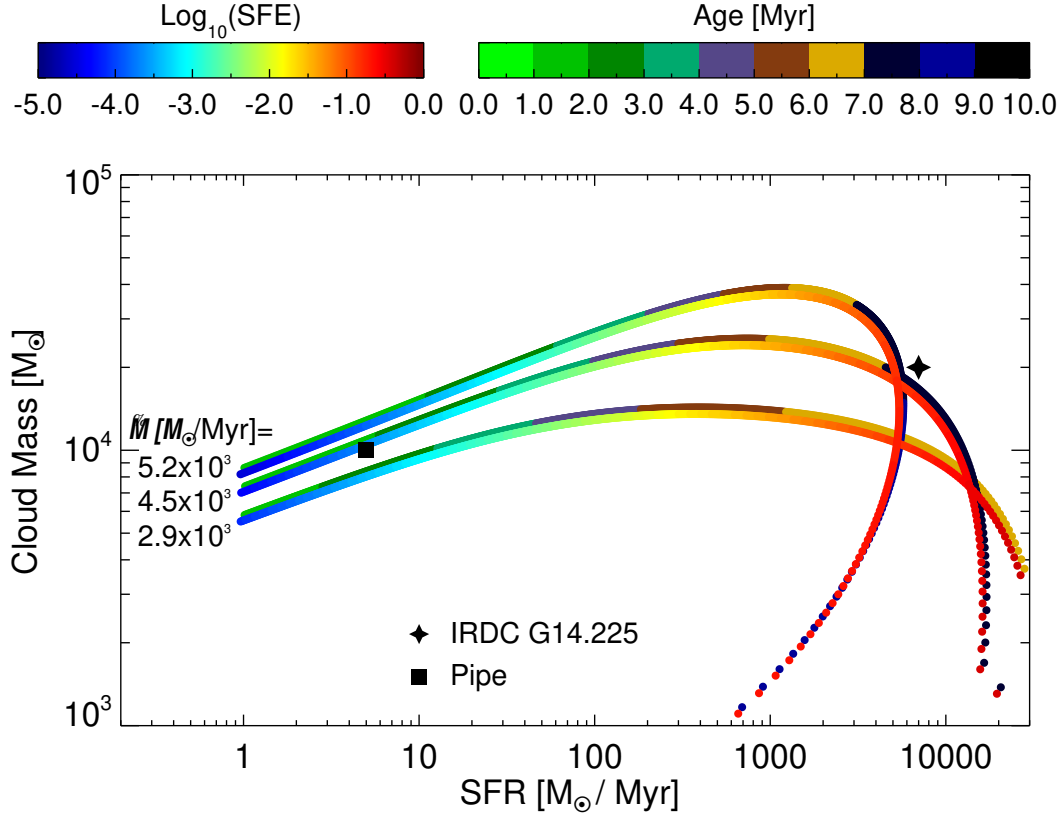


**Figure 13.** Analytical model for the evolution of clouds with different accretion rates in a cloud mass *versus* SFR diagram (Vázquez-Semadeni et al. 2018). The tracks show the instantaneous mass and SFR for the different accretion rates. The symbols correspond to the loci of the Pipe and G14 clouds in this diagram. Each track is shown in two color scales representing the cloud age and its SFE. Note that at  $\sim 6$  Myr all models reach its maximum mass and then the cloud mass decreases and the SFR decelerates due mainly to effects of ionizing radiation from massive stars.

star-forming activity even when normalized to the total cloud mass. Additionally, a recent study by Shimoikura et al. (2019) reported a SFE 9–17% for the M17 S Wex. This study, conducted on  $\text{N}_2\text{H}^+$ , concluded that according to the density profile of the cores, more than 80% of their sample is consistent with the free-fall condition. This result reinforced our evolutionary scenario in terms of the gravitational collapse.

#### 4.3. Comparison with an analytical model

We use the model presented by Zamora-Avilés et al. (2012, see also Zamora-Avilés & Vázquez-Semadeni, 2014), which describes the evolution of clouds with different masses, to compute the evolution for G14, as shown for several clouds in Vázquez-Semadeni et al. (2018). The model starts with a cloud formed by converging streams in the warm neutral medium (WNM). The cloud mass grows due to accretion at constant density until it reaches its Jeans mass and starts to collapse. The collapse is solved self-consistently during the evolution of the cloud. As this happens, the mean density and mass fraction at

high density increase, implying an increase of the SFR. Thus, the model is able to describe, as a function of time, and parameterized by the maximum mass attained by the cloud during its evolution, the SFR, SFE, mass and mean density of clouds in global gravitational contraction. The model predicts that, during the early stages of a cloud’s evolution, the mass, density and SFR increase monotonically, while the radius decreases. Therefore, during this period, any of these quantities can be used as a proxy for time. For the present work, the model has been parameterized by the accretion rate onto the cloud. We consider models with mass accretion rates  $\dot{M} = 2.9, 4.5, 5.2 \times 10^3 M_{\odot} \text{Myr}^{-1}$ , in order to increase the mass of the cloud by amounts comparable to the mass difference between G14 and the Pipe. Figure 13 shows a diagram of instantaneous cloud mass vs. SFR, where the SFR is taken as the proxy for time. In this diagram, we show evolutionary tracks for the clouds with the various accretion rates. It can be seen in this figure that the evolutionary track for the cloud with  $\dot{M} = 4.5 \times 10^3 M_{\odot} \text{Myr}^{-1}$  passes nearest the two loci of the Pipe and G14 in

this diagram. However, it takes the model  $\sim 5$  Myr to go from a Pipe-like stage to a G14-like stage. In the simulation, 2 Myr are enough to observe this transition. However, we should take into account that the evolution of the simulated clump is representative of the substructure in both observed clouds, such as their clumps and filaments, and not to the clouds themselves. Then, the estimation of the model presented in this section is in qualitative agreement with the results from the simulation, and reinforcing the suggestion that the Pipe would evolve into a G14-like stage in the course of some megayears if the Pipe were embedded in an environment similar to that of G14.

According to the model (see Fig. 13) the evolution of G14 is consistent with our prediction based on the energy budget evolution observed in the  $\mathcal{L} - \Sigma$  diagram. These two evolutionary predictions show that low-mass clouds are able to evolve to high mass regions in a few Myr if their external mass accretion rate is large enough.

## 5. DISCUSSION

### 5.1. Implications

The evolution of the numerical clump sample studied in this work is consistent with the analytical calculations presented in BP+18, in the sense that the clumps evolve in the  $\mathcal{L} - \Sigma$  diagram from the sub-virial region to the energy equipartition region, similarly to the evolution predicted by eq. (7).<sup>12</sup> However, the clumps in the present study show a slightly different behavior. In our case, the clumps approach the equipartition lines almost perpendicularly to them, while the prediction is that they should approach these lines asymptotically (cf. eq. (7) and the left panel of Fig. 1 of BP+18). Moreover, the column density of our clumps does not increase monotonically over time, as in Fig. 1 of BP+18, but rather decreases again at late stages during the clumps' evolution (see top panels of Figs. 7 and 8). This difference is mainly due to the definition of the clumps employed in each case. In our numerical sample, clumps are defined as connected regions above fixed thresholds in the density field. This definition implies that the clumps are free to vary in size and mass throughout their evo-

lution, while in BP+18 clumps have constant mass by construction. Additionally, the prescription of sink formation above a certain critical density precludes the formation of regions with density above the critical sink-formation value. Then, as the clumps evolve, they become denser until sink formation becomes significant. On the other hand, the analytical treatment in BP+18 simply follows spherical, constant-mass clumps as they collapse and increase their column density. Moreover, loss of gaseous mass to star formation is not considered in the analytical treatment of BP+18. Therefore, in this idealized setting, clumps can only decrease their volume and increase their column densities as they collapse. Instead, our numerical clumps can lose mass by forming sinks, and when they do, their density and column density decrease. Therefore, their evolutionary tracks in the  $\mathcal{L} - \Sigma$  diagram differ from the analytical treatment, as also observed in the numerical core sample considered by BP+18, which describes paths in the  $\mathcal{L} - \Sigma$  diagram similar to those of our own sample, characterized by a turnaround. On the other hand, the data from our numerical clumps and cores are also consistent with the observational data. Early in their evolution, the substructure in the numerical cloud exhibits a low column density, in the same range as that of the cores in the Pipe cloud, which is thought to be at an early evolutionary stage. Similarly, at later times, the substructure in the numerical cloud occupies the same  $\Sigma$  range as the substructures in the G14 cloud.

Another important point to notice is that the ensemble of clumps in our simulation does contain a fraction of super-virial clumps at low column densities in the  $\mathcal{L} - \Sigma$  diagram, or low masses in the  $\alpha - M$  diagram, similarly to the case of observational surveys (e.g., Kauffmann et al. 2013; Leroy et al. 2015). This was interpreted in Camacho et al. (2016) and BP+18 as a consequence of those clumps being either in a dispersal state, or in an assembly stage by external (non-self-gravitating, or “inertial”) compressions or by a large-scale potential well which drag them gravitationally. In neither case do the inertial motions (by “turbulence” or by an external gravitational field) provide support for the clumps to be in a near-equilibrium state, and so, for super-virial clumps, there is no need for an external confining thermal pressure. However, for clumps undergoing assembly (roughly half of the clump population; Camacho et al. 2016), the inflow may effectively be considered as a “confining” ram pressure for the densest material. A large range of  $\alpha$ , from sub- to super-virial, is also observed in our sample of cores in the Pipe. Despite being in the low- $\Sigma$  range, roughly half of the Pipe cores show high- $\alpha$  values, which, as discussed above, can be an indicator of assembling or dispersing motions, rather than a confining pressure.

As discussed by Camacho et al. (2016) and BP+18, the

<sup>12</sup> In a recent numerical study, Padoan et al. (2016) suggest that clumps follow the standard Larson linewidth-size relation, regardless of the column density. However, on the one hand, this study has been performed in a numerical simulation with supernova driving into a closed box of size 256 pc per side, which does not allow the hot gas to escape to high altitude above the galactic plane, thus raising concerns that their numerical box is over-driven, as discussed in Camacho et al. (2016). On the other hand, the column densities of the clumps considered by Padoan et al. (2016) are rather low ( $\Sigma \lesssim 100 M_{\odot} \text{ pc}^{-2}$ ), and still coincide with the range where indeed little or no correlation between  $\mathcal{L}$  and  $\Sigma$  is observed (e.g., Leroy et al. 2015; Traficante et al. 2018a). It is unclear whether clumps in Padoan et al. (2016) with densities  $\Sigma \gtrsim 100 M_{\odot} \text{ pc}^{-2}$ , comparable to those in G14, will anyway exhibit the expected  $\mathcal{L} - \Sigma$  trend.

starting location in the  $\mathcal{L}-\Sigma$  diagram of clumps undergoing inertial assembly must appear as super-virial, since, by definition, the inertial assembly speed for these objects is larger than their self-gravitating speed,  $\sigma_g$ , given by eq. (5). Later, as the clump becomes denser and more massive, and its self-gravitating speed increases, the latter eventually becomes larger than the assembly speed, and the clump may appear to be either in equipartition or sub-virial when it becomes dominated by self-gravity. In particular, it will appear sub-virial if  $\sigma_g$  is still smaller than the equipartition value  $\sigma_{\text{eq}} \equiv \sqrt{\eta GM/R}$ , because  $R$  is still not sufficiently smaller than  $R_0$  (upper solid lines in the left panel of Fig. 1 of BP+18). On the other hand, clumps can exhibit sub-virial Larson ratio or virial parameter during the early stages of their contraction if their initial internal turbulent velocity is low, and their infall speed has not yet reached the free-fall value (Ballesteros-Paredes et al. 2018). In addition, Traficante et al. (2018b) have suggested that a sub-virial appearance can also occur in observations as a consequence of a mismatch between the regions from which the mass and the velocity dispersion are derived, if these are selected using different tracers. However, this effect cannot be at play for the data from our simulation, in which the clump properties are measured directly from the numerical data, and therefore their sub-virial nature has to be a real physical property.

The fact that the numerical clumps investigated in this work initiate their trajectories in the sub-virial region of the  $\mathcal{L}-\Sigma$  and  $\alpha-M$  diagrams indicates that they are already dominated by self-gravity, yet they have not had time to attain the equipartition speed, since equipartition is only attained at later times in their evolution, as shown by Figs. 11 and 12. In the observational sample, this increasing- $\alpha$  evolutionary trend is shown by the absence of sub-virial objects in the G14 cloud.

It is important to note also that, were we to follow the evolution of our numerical clumps to even more advanced stages, they would move into the super-virial region, since they would have lost a large amount of mass to sink formation, therefore losing gravitational energy from the gas mass, but the velocity dispersion would remain roughly the same. Therefore, they would appear to be super-virial. In Camacho et al. (2016) we showed that some apparently super-virial clumps could be made to appear in equipartition again when the mass in sinks was included in the computation of the kinetic to gravitational energy balance. Finally, this effect would also occur if feedback were included, because in this case mass would be lost from the clumps due to the feedback, also reducing their gravitational content. Thus, apparently super-virial clumps are likely to occur once a significant amount of their gas mass has been converted to stars and/or feedback has expelled a significant amount

of mass from them. All of this, aside from geometrical effects such as those discussed by BP+18.<sup>13</sup>

Finally, as mentioned above, we have been able to interpret the physical properties and star formation activity of two different star forming regions as a consequence of evolutionary effects that transform one into the other in a simulation including only decaying turbulence and self-gravity.

## 5.2. Caveats

The simulation presented in this work clearly lacks important physical ingredients, most notably, stellar feedback and magnetic fields. The omission of stellar feedback, however, is probably not a major concern, as discussed in detail in Appendix C. Indeed, our region of study (“Region A”) has been chosen to be far from any regions harboring massive stars that could produce supernova remnants capable of disturbing the region at the time studied, and at a time in its evolution at which no massive stars have formed yet that could affect it by photoionizing radiation. Feedback from low-mass stars is well known to possibly affect the structure only on  $\sim 1$  pc scales (e.g., Bally 2016), but not at the cloud scales,  $\sim 10$  pc.

For the same reason, we avoid using artificial turbulence driving (generated, for example, in Fourier space). On the one hand, Appendix B shows that our region is unlikely to be affected by feedback during the time interval in which we study it. On the other hand, even if feedback had to be included, Fourier driving is rather inadequate as a substitute, since it is applied everywhere in space and nearly continuously in time, rather than intermittently in both time and space, as real stellar feedback is.

Concerning the magnetic field, it is now well established that most clouds and dense cores are magnetically supercritical (e.g., Crutcher 2012), and thus evolve under the domination of self-gravity, although the presence of a weak field could still slow down the gravitational contraction. We plan to repeat our study in the presence of a magnetic field in a future paper.

On the other hand, in spite of the above limitations, our simulation considers features that are usually neglected in numerical studies of molecular clumps. Most importantly, it follows the self-consistent evolution of the clump since the formation of the cloud complex it belongs to, thus allowing for the growth and continued accretion onto the clump, which regulate its physical properties and star formation activity. This is the reason why our

<sup>13</sup> In BP+18 it was shown that  $\alpha$  computed with the standard definition given by the second equality of eq. (1) can often overestimate the true value of the energy ratio, because it assumes that the gravitational energy is given by the expression for uniform density sphere, which is smaller than the true gravitational energy of a centrally concentrated object.

study focuses on a time more than 20 Myr after the start of the simulation, since it has been previously necessary for the parent cloud complex to form and grow from the warm diffuse gas, and then engage in global gravitational contraction, which is the essence of the GHC scenario. The clump itself follows a similar path at its own scale. This self-consistent evolution cannot be followed by simulations of isolated, isothermal regions over short time spans. We consider that this setup is ideally suited for studying the early evolution of clumps undergoing GHC.

## 6. SUMMARY

In this work we have presented a study of the energy budget of a star-forming clump in a numerical simulation in which many cloud complexes form by global hierarchical collapse, and compared the numerical results to data from two real clouds (Pipe and G14). The clumps studied in this work, both from the simulation and from the observational data, lie close to the energy equipartition relation, shown in the  $\mathcal{L} - \Sigma$  diagram. This trend has been approximately found in several previous observational and numerical studies (Keto & Myers 1986; Heyer et al. 2009; Dobbs et al. 2011; Leroy et al. 2015; Traficante et al. 2015; Camacho et al. 2016; Ballesteros-Paredes et al. 2018). However, deviations from it are also systematically observed. In this study, we suggest that these deviations are characteristic of the clump evolutionary state, and that this evolution determines also the star formation activity of the clumps.

The main result from the present study is that our numerical clump evolves from a Pipe-like state to a G14 one in roughly 2 Myr. The Pipe-like stage is characterized by a lower mass, velocity dispersion, mean and peak densities, and star formation activity, while maintaining comparable dimensions. The increase in physical parameters is due to accretion of material external to the  $n_{\text{th}} = 10^3 \text{ cm}^{-3}$  boundary we used to define this clump, as indicated by the fact that the time delay for the appearance of the first stars after the time at which we first observe the clump is within  $\sim 10\%$  of the free-fall time for the clump at the starting time. In addition, a comparison with the analytical model by Zamora-Avilés & Vázquez-Semadeni (2014), which describes the evolution of the physical parameters and star-forming activity of a gravitationally contracting cloud, using initial parameters appropriate for the Pipe cloud, shows that a G14-like cloud (in mass and SFR) appears roughly a few Myr later. These results strongly suggest that clouds evolve from low-mass, low-density, and low-SFR states to states of higher masses, densities and SFRs over the course of a few megayears if their external mass accretion rate is large enough.

This evolution of the clouds implies an evolution of the energy budget of their substructures, so that samples of

cores of younger clouds appear displaced toward more sub-virial states in the  $\mathcal{L} - \Sigma$  and  $\alpha - M$  diagrams, and, as the clouds age, their structures are displaced in these diagrams towards higher-column densities and closer to equipartition, due to the mechanism described in BP+18 and Vázquez-Semadeni et al. (2019), which predicts that the Larson ratio and the virial parameter of cores that decouple from the global flow and begin to contract at a finite radius  $R_0$  evolve during the core's contraction. The details of the evolution depend on the initial ratio of the inertial external compressions to the self-gravity-driven motions approaching the equipartition values as collapse proceeds and the inertial motions become subdominant (see Fig. 2 of Vázquez-Semadeni et al. 2019). Nevertheless, at late stages, coeval samples of clumps and cores exhibit the regularly-observed feature that more massive objects have lower values of  $\alpha$ . Vázquez-Semadeni et al. (2019) have suggested that the lower  $\alpha$  of more massive objects may arise as a consequence of them having lower average densities, and therefore longer free-fall times, causing them to evolve more slowly in their approach to equipartition.

Our results lead us to suggest that massive dense cores that appear sub-virial and quiescent (i.e., prestellar or very weakly-star-forming cores; e.g., Kauffmann et al. 2013; Liu et al. 2015; Ohashi et al. 2016; Sanhueza et al. 2017; Contreras et al. 2018) will evolve toward equipartition as they develop stronger star-formation activity. Also, since we found that, at early stages, the densest parts of the clumps appear more sub-virial than their envelopes, we predict that observations of the parent clumps of those sub-virial cores should reveal that the parent structures are closer to equipartition.

## ACKNOWLEDGMENTS

The authors thank the anonymous referee for the useful comments that helped to improve this work. V.C. acknowledges support from CONACyT grant 406297. V.C. and EVS are thankful to the project CB-2015-255295 supported by CONACyT. A.P. acknowledges financial support from UNAM-PAPIIT IN113119 grant, México. G.B. is supported by the MINECO (Spain) AYA2017-84390-C2 grant. M.Z.A. acknowledges support from CONACyT grant number A1-S-54450 to Abraham Luna Castellanos (INAOE).

*Software:* Astrodendro (<https://github.com/dendrograms/astrodendro>), Astropy (<http://www.astropy.org>, Astropy Collaboration et al. 2013, 2018) CASA (McMullin et al. 2007), GADGET2 (Springel 2005), GILDAS ([www.iram.fr/IRAMFR/GILDAS](http://www.iram.fr/IRAMFR/GILDAS), Pety 2005, GILDAS team 2013).

## APPENDIX

## A. TESTING DENDROGRAM PARAMETERS

As described in Sec. 3.2, for selecting the structures in G14 we used the `dendrogram` algorithm. However, the objects defined by this algorithm depend heavily on the values of the parameters chosen (e.g., Goodman et al. 2009; Burkhart et al. 2013). Specifically, two crucial parameters are `min_value` and `min_delta`. These respectively define the minimum intensity value above which structures are searched and the “tolerance” allowed for fluctuations above a certain level to identify a structure as an independent one. Thus, `min_value` is equivalent to the density threshold we use to define objects in the simulation and *defines the class of object being considered*. That is, successively higher values of `min_value` allow defining clouds, filaments, clumps or cores. On the other hand, `min_delta` determines how strong a neighboring peak needs to be to be classified as a separate structure. In particular, this determines whether moderate-amplitude fluctuations around a large structure are interpreted as separate structures or incorporated into it. That is, this parameter determines whether a given structure “branches out” into smaller ones or not. In turn, this causes the isocontours of a given large structure to increase in size when `min_delta` is increased, since the structure will then incorporate additional minor structures around it. This non-uniqueness of the isocontours that can be defined by the `dendrogram` algorithm is a direct consequence of the attempt to define isolated objects amid a continuous medium. Therefore, the question arises<sup>14</sup> as to what is the uncertainty in the values of the virial parameter and the Larson ratio introduced by the ambiguity in the definition of the structures.

To estimate the uncertainty in our results introduced by the choice of parameters, in this Appendix we consider an alternate choice of the `min_delta` parameter, which affects the isocontours of the structures we identified in G14. We do not vary `min_value`, since it only determines the class of object, and is thus as arbitrary as our choice of density threshold for the simulation data.

In Sec. 3.2 we discussed the selection of the `min_value` and `min_delta` values for each of the defined kind of objects: cores, clumps, and filaments, which are  $(\mathbf{n}_v, \mathbf{n}_d) = (15,3)$ ,  $(5,1)$ , and  $(1,1)$  respectively. We will refer to this set of structures as Sample I. For the test, we now choose a fixed value  $\mathbf{n}_d=5$  for each class in order to reduce the branching. Given that `min_value` remains the same as in Sample I, the increase of `min_delta` produces a new set of objects, which we refer to as Sample II. From it, we select a subgroup of objects related to those of Sample I (see Fig. 14), to investigate how their properties change.

To explore the differences between the same kinds of objects, we show in Fig. 14 the contours defined by `dendrogram` in the original G14 sample (Sample I; solid lines) and those obtained with the new value of `min_delta` (Sample II; dotted lines). The labels are the same as in Fig. 2 for the objects in Sample I, while those from Sample II are labeled with the same name with an apostrophe for those objects having a counterpart in Sample I, and with a letter for those that are different. It can be noticed in Fig. 14 that objects in panels (a) and (f), and object “Co2” in panel (e) have nearly the same contours in both samples, which indicates that these compact objects do not depend significantly on the value of `min_delta`. This is because the density profile in these objects is very steep, and no new material is incorporated into them by increasing `min_delta`. On the contrary, the rest of the objects in Sample II show significant variations in their contours. In particular, note that many of the peripheral structures from Sample I are incorporated into objects from Sample II. For example, filament “fa” from Sample II contains filaments “f1” and “f2” from Sample I, while clump “CA” in Sample II contains clumps “C8– to “C11” from Sample I. Also, the counterparts of “f3” and “C7”, in the new sample include small structures discarded in Sample I.

From the images in Fig. 14, it is clear that the increment in `min_del` causes the small structure to be absorbed in the new sample, see for example, “f3” and “C7”. Another effect when changing this parameter is the generation of a new hierarchy of objects, for example “CA”, which has been defined with the `min_value` for clumps in Sample I, but with the new `min_del`, it should be defined as a filament. Thus, it is expected that their corresponding physical properties, in particular  $\mathcal{L}$  and  $\alpha$ , must change.

To investigate the effect of a different defining criterion for the objects on the values of the Larson ratio and the virial parameter, Fig. 15 shows the  $\mathcal{L} - \Sigma$  (left panel) and  $\alpha$  (right panel) plots for the clumps from Sample I (blue circles) and the new objects from Sample II (orange stars). It is readily seen from this figure that the objects from Sample II, in both the  $\mathcal{L} - \Sigma$  and  $\alpha - M$  plots, occupy the same locus as those from Sample I. In addition, Fig. 16 shows the  $\mathcal{L} - \Sigma$  plot (left panels) and  $\alpha$  plot (right panels) for selected individual objects in Sample I (blue circles) and their counterparts in Sample II (orange stars). Note that, as described above, some of the objects in Sample II incorporate several objects from Sample I, so the correspondence is not necessarily one-to-one. In particular, it is seen that a new object in Sample II sometimes comprises several smaller objects from Sample I, and in this case, it is more resemblant

<sup>14</sup> We thank the referee for pointing this out.

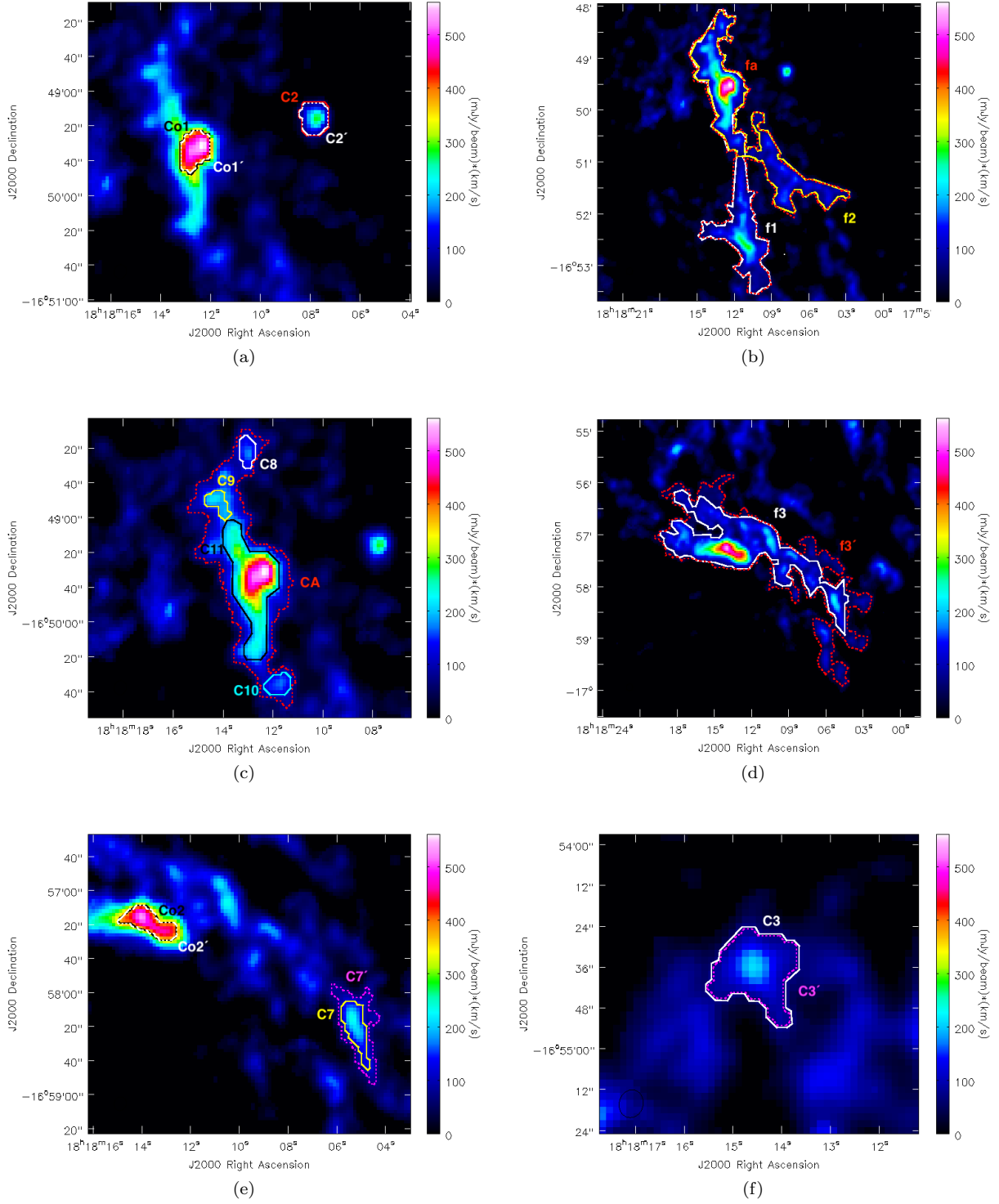


Figure A14.: Comparison between the original G14 sample (solid lines) and the structures obtained with  $\text{min\_del} = 5\sigma$  (dotted lines).

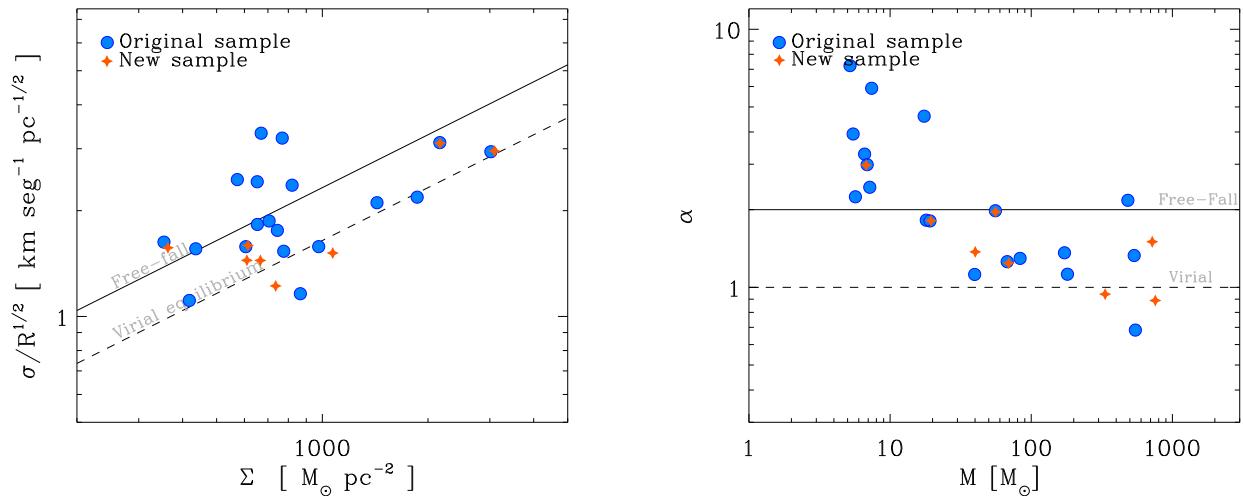


Figure A15.:  $\mathcal{L} - \Sigma$  plot (left panel) and  $\alpha$  plot (right panel) for the original G14 sample (Sample I, blue circles) and the new structures obtained with `min_delta`=  $5\sigma$  (Sample II, orange stars). Both samples are located in the same locus, suggesting that there is no significant qualitative variation when changing the `dendrogram` input parameters.

of a larger-scale class of objects. This is the case, for example of clump CA from Sample II, which engulfs clumps C8-C11 from Sample I (see the panels in the second row of Fig. 16), and is thus more similar to filaments f1 and f2 in Sample I. But it is seen in this case that clump CA is located nearer to the loci of filaments f1 and f2 than to the loci of the smaller clumps C8-C11. Therefore, when the effect of the change in `min_delta` changes the category of the resulting object (from clump to filament, for example), the values of  $\mathcal{L}$  and  $\alpha$  for the new object are consistent with the values for objects of the same category in the old sample.

We thus conclude that, rather than introducing an “uncertainty” in the values of  $\mathcal{L}$  and  $\alpha$ , varying the `min_delta` parameter simply changes the object defined for study, with the consequent change in its physical properties. This is fundamentally a consequence of attempting to define discrete objects within a continuous medium, so that when the defining criterion is changed, the resulting object defined also changes essentially. However, because the original sample contained objects of several classes (i.e., defined with different values of the `min_value` parameter), the changes in the object introduced by changing `min_delta` can at most change its classification, but it continues to be located within the locus of the full sample of objects originally defined in Sample I. Thus, our results are insensitive to variations in the parameters of the `dendrogram` algorithm.

## B. COMPARISON WITH THE AMMONIA DATA

In this work we report the results for the G14 sample from the data obtained directly from the  $\text{H}_2$  column density map (Lin et al. 2017). However, the data of the  $\text{NH}_3$  (1,1) and (2,2) lines (Busquet et al. 2013) allow as well the estimation of the column density,  $N(\text{H}_2)$ , by applying the radiative transfer equations (see below). In what follows we show the comparison of  $N(\text{H}_2)$  and the mass derived with the ammonia data and the  $\text{H}_2$  column density map of Lin et al. (2017).

For the computation of the physical parameters, we extracted the spectrum from the contours defined with the `dendrogram` using the CASA software for both the (1,1) and (2,2) lines. We analyze the spectra with the CLASS ammonia method in GILDAS<sup>15</sup>. This method takes into account the hyperfine structure of ammonia. It computes the ammonia line profiles assuming a Gaussian velocity distribution and equal excitation temperatures. Then, we follow the procedure in Busquet et al. (2009) in order to derive the column density. Table 3 shows the data for the  $\text{NH}_3$  column density derived following Busquet et al. (2009) and the column density measured directly from the  $\text{H}_2$  map (Lin et al. 2017).

<sup>15</sup> <http://www.iram.fr/IRAMFR/GILDAS>

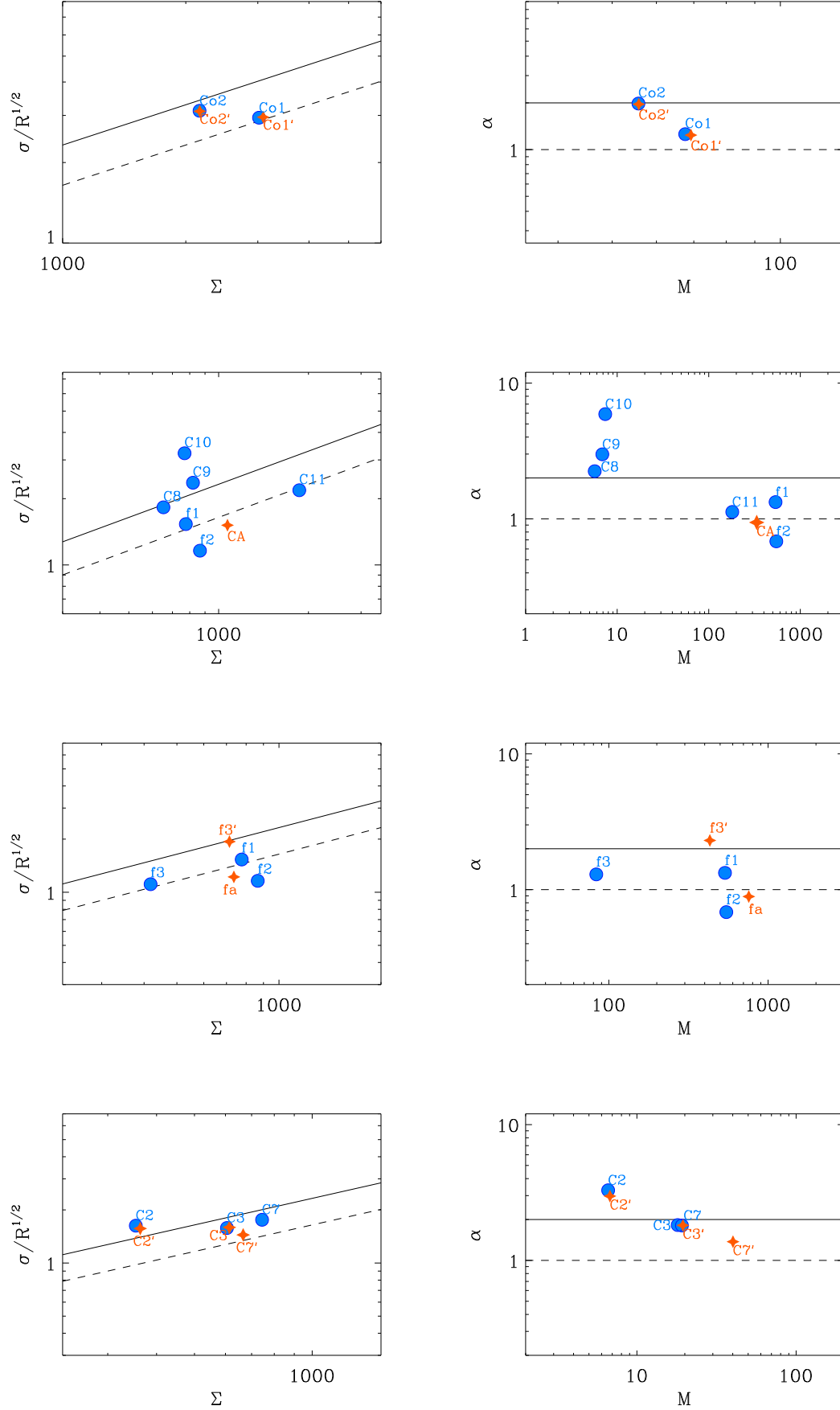


Figure A16:  $\alpha$  comparison between the original G14 objects (blue circles) and the new sample (orange stars). The units are the same as  $s$  in Fig. 15 and the lines represent the free fall (continue) and the virial equilibrium (dashed) conditions.

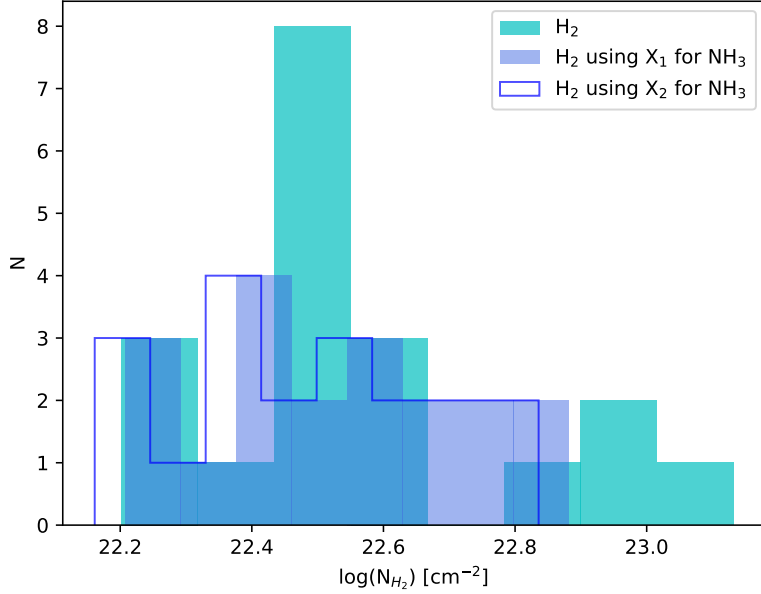


Figure B17:  $H_2$  column density derived from the  $H_2$  map (Lin et al. 2017) and from the  $NH_3$  maps (Busquet et al. 2013) using two different abundances,  $X_1 = 4.2 \times 10^{-8}$  (Sánchez-Monge et al. 2013) and  $X_2 = 4.7 \times 10^{-8}$  (this work).

ID	R (pc)	$N(NH_3)$ $10^{14} \text{cm}^{-2}$	$N(H_2)$ $10^{22} \text{cm}^{-2}$
C1	0.079	7.26	1.95
C2	0.084	14.49	1.58
C3	0.109	18.59	2.71
C4	0.107	31.99	2.57
C5	0.054	11.48	3.00
C6	0.056	30.56	2.93
C7	0.096	25.32	3.34
C8	0.057	9.08	2.93
C9	0.056	10.52	3.68
C10	0.060	16.69	3.45
C11	0.191	14.80	8.36
C12	0.124	10.01	4.38
C13	0.213	15.05	6.42
c1	0.092	20.72	13.56
c2	0.099	22.78	9.70
f1	0.511	6.76	3.48
f2	0.488	7.21	3.88
f3	0.274	10.60	1.87
f4	0.509	13.80	3.16

Table B3: Column density from the ammonia and the  $H_2$  maps for the G14 sample defined with dendrograms.

$$X_2 = \frac{N(NH_3)}{N(H_2)} = 4.7 \times 10^{-8}, \quad (\text{B1})$$

In order to compute the  $N(H_2)$  column density from the ammonia data we need to assume an abundance,  $X(NH_3)$ . One adopted value in the literature, obtained as an average of several samples is  $X_1 = 4.2 \times 10^{-8}$  (Sánchez-Monge et al. 2013, and references therein). However, given the  $NH_3$  and  $H_2$  column densities, we can compute the  $NH_3$

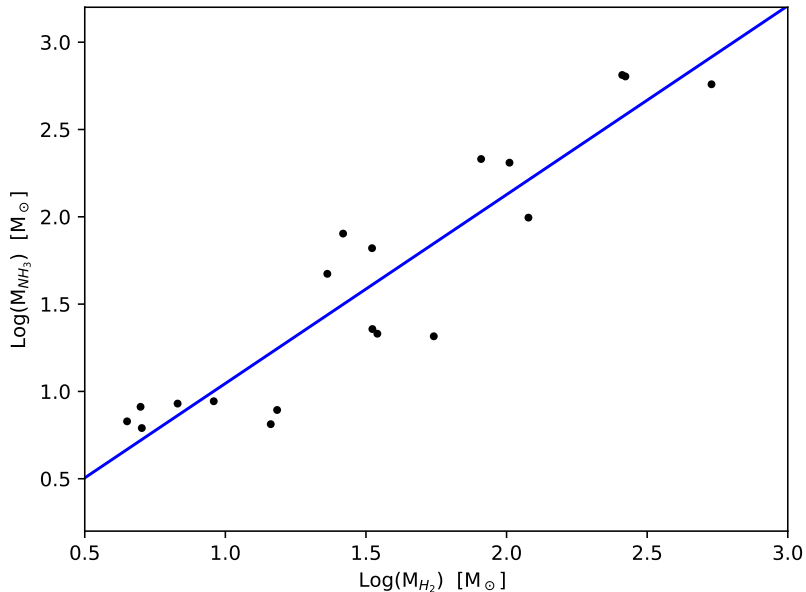


Figure B18: Comparison of the objects’ mass measured through the  $\text{NH}_3$  data (using  $X_1 = 4.2 \times 10^{-8}$ ) and directly from the  $\text{H}_2$  map. The blue line corresponds to the fit, which has a slope of 1.08, showing a good correlation for the mass measurements with the different tracers.

abundance for G14, considering the values in Tab. 3. Figure 17 shows the comparison for the  $\text{H}_2$  column density obtained directly from the  $\text{H}_2$  map of Lin et al. (2017), the  $\text{H}_2$  column density obtained using the abundance reported in Sánchez-Monge et al. (2013) and the one obtained using the abundance derived in this work. The mass for our G14 sample was computed considering  $X_1$ . Figure 18 shows the comparison between the masses derived from  $\text{NH}_3$  and the  $\text{H}_2$  maps. We found quite similar and consistent masses using both independent methods.

### C. ESTIMATING THE IMPACT OF NEGLECTING STELLAR FEEDBACK

As mentioned in Sec. 5.2, our simulation does not include any form of stellar feedback. Here we estimate the likely impact of this omission in the realism of our “numerical cloud”. An important consideration in this regard is that the masses of the sink particles allow us to estimate the masses of the typical stars acting on the cloud, and these masses increase over time, representing the growth of the stellar cluster formed by the cloud. Indeed, although our simulation lasts 34 Myr, during an important fraction of that time there is no star formation. The first sink forms only at  $t \sim 16$  Myr, with a mass  $\sim 12M_\odot$ , and in a region  $\sim 60$  pc from region A. In the region A itself, the first local sink appears at  $t \sim 21.6$  Myr, with mass  $\sim 3M_\odot$ . For comparison, we study our cloud within region A in the time interval from  $t_i = 20.3$  Myr to  $t_f = 22.1$  Myr, so that, in fact, the region contains no stars at the beginning of our study.

We now evaluate the impact of omitting stellar feedback. If feedback were present, it would have to affect the dynamics of the cloud during the  $\sim 2$  Myr we are studying. Some of the most important possible sources of feedback are, from weakest to strongest, *i*) outflows, *ii*) photoionizing radiation, and *iii*) supernovae. Concerning outflows, it is generally agreed that outflows from low-mass YSOs only affect their immediate surroundings, up to distances  $\lesssim 1$  pc, but hardly affect their entire parent MC (Bally 2016, and references therein). Moreover, even in the presence of outflows, the accretion flow onto the cores and YSOs is not prevented (e.g. Wang et al. 2010) and, in fact, the outflows last only as long as the accretion does (Bally 2016). On the other hand, although very massive sources are able to provide powerful outflows that extend over tens of parsecs, they still cannot halt most clumps (Bally 2016). Thus, we can discard outflows as relevant for our study. Several numerical studies (e.g., Gavagnin et al. 2017; Vázquez-Semadeni et al. 2017; Dale 2017; Grudić et al. 2019) also support the suggestion that feedback at the cloud scale is dominated by massive stars, but these appear a few Myr after the onset of SF in the cloud. In further support of this conclusion, we note that the simulations presented in González-Samaniego & Vázquez-Semadeni (2020), which do include stellar feedback and are performed with a grid code, the general evolution of clouds with and without feedback is nearly identical until a very massive ( $\sim 20M_\odot$ ) star forms.

Concerning photoionization and SNe, we can estimate the severity of the omission as follows. Applying a standard IMF to our sink particles, we find that, at  $t = t_f$ , the most massive star that can be hosted by the most massive sink in our cloud would have a mass  $\sim 4M_\odot$ . If we consider all the sink particles within our region then the most massive star may have  $\sim 7M_\odot$ . Such a star does not produce significant photoionizing radiation and does not explode as a SN in at least  $\sim 30$  Myr.

A nonlocal SN explosion could still affect our cloud if it occurs sufficiently nearby in space and time. The nearest star-forming region is  $\sim 60$  pc away, and it started forming stars  $\sim 6$  Myr before  $t_i$ . For a SN in this region to impact our cloud, it should explode during this 6-Myr interval. For this to happen, the star should have a mass of at least  $20M_\odot$ . Again applying the standard IMF, a sink must have  $2000 M_\odot$  to form at least one  $20M_\odot$  star. However, at  $t = t_i$ , the neighbouring cluster has a total mass of only  $\sim 1550M_\odot$ , which is not enough to form a  $20M_\odot$  star. Conversely, it only reaches a total mass of  $\sim 2000M_\odot$  at  $t \sim 21.6$  Myr, the moment when the first sink particle appears in the cloud. We stop the analysis just 0.5 Myr after that. Thus, even though the neighboring region eventually reaches a sufficiently large mass to form the required massive star, it does not have time to interact with our region.

Finally, a last possibility exists: that of a passing Type Ia SN, that could explode in the neighborhood of our cloud. The standard estimate is that a given cloud is hit by a SN shock roughly once every 1 Myr (McKee & Ostriker 1977). So, at most, during the evolution of our cloud, one SN shock may pass through it. However, in order for it to cause much damage to the cloud, the SN must explode inside it, while external explosions cause very little damage (e.g. Iffrig & Hennebelle 2015). Therefore, we conclude that the omission of stellar feedback does not pose a significant problem for the evolution of our clouds dynamics.

## REFERENCES

- Abel, T. 2011, MNRAS, 413, 271
- Alves, F. O., & Franco, G. A. P. 2007, A&A, 470, 597
- Alves, J., Lombardi, M., & Lada, C. J. 2007, A&A, 462, L17
- Ascenso, J., Lada, C. J., Alves, J., Román-Zúñiga, C. G., & Lombardi, M. 2013, A&A, 549, A135
- Astropy Collaboration, Robitaille, T. P., Tollerud, E. J., et al. 2013, A&A, 558, A33
- Astropy Collaboration, Price-Whelan, A. M., Sipócz, B. M., et al. 2018, AJ, 156, 123
- Ballesteros-Paredes, J. 2006, MNRAS, 372, 443
- Ballesteros-Paredes, J., Klessen, R. S., Mac Low, M.-M., & Vázquez-Semadeni, E. 2007, Protostars and Planets V, & Ballesteros-Paredes, J., Hartmann, L. W., Vázquez-Semadeni, E., Heitsch, F., & Zamora-Avilés, M. A. 2011, MNRAS, 411, 65
- Ballesteros-Paredes, J., & Mac Low, M.-M. 2002, ApJ, 570, 734
- Ballesteros-Paredes, J., Vázquez-Semadeni, E., & Scalo, J. 1999, ApJ, 515, 286
- Ballesteros-Paredes, J., Vázquez-Semadeni, E., Palau, A., & Klessen, R. S. 2018, MNRAS, 479, 2112 (BP+18)
- Bally, J. 2016, ARA&A, 54, 491
- Banerjee, R., Vázquez-Semadeni, E., Hennebelle, P., & Klessen, R. S. 2009, MNRAS, 398, 1082
- Bate, M. R. 2009, MNRAS, 392, 1363
- Bertoldi, F., & McKee, C. F. 1992, ApJ, 395, 140
- Boulares, A., & Cox, D. P. 1990, ApJ, 365, 544
- Brooke, T. Y., Huard, T. L., Bourke, T. L., et al. 2007, ApJ, 655, 364
- Burkhart, B., Lazarian, A., Goodman, A., et al. 2013, ApJ, 770, 141
- Busquet, G., Palau, A., Estalella, R., et al. 2009, A&A, 506, 1183
- Busquet, G., Zhang, Q., Palau, A., et al. 2013, ApJL, 764, L26
- Busquet, G., Estalella, R., Palau, A., et al. 2016, ApJ, 819, 139
- Caldwell, S., & Chang, P. 2018, MNRAS, 474, 4818
- Camacho, V., Vázquez-Semadeni, E., Ballesteros-Paredes, J., et al. 2016, ApJ, 833, 113
- Carroll-Nellenback, J. J., Frank, A., & Heitsch, F. 2014, ApJ, 790, 37
- Chen, H.-R. V., Zhang, Q., Wright, M. C. H., et al. 2019, arXiv e-prints, arXiv:1903.04376.
- Collins, D. C., Kritsuk, A. G., Padoan, P., et al. 2012, ApJ, 750, 13
- Contreras, Y., Sanhueza, P., Jackson, J. M., et al. 2018, ApJ, 861, 14
- Crutcher, R. M. 2012, ARA&A, 50, 29
- Dale, J. E. 2017, MNRAS, 467, 1067
- Dib, S., Kim, J., Vázquez-Semadeni, E., Burkert, A., & Shadmehri, M. 2007, ApJ, 661, 262
- Dobbs, C. L., Burkert, A., & Pringle, J. E. 2011, MNRAS, 413, 2935
- Dzib, S. A., Rodríguez, L. F., Araudo, A. T., et al. 2013, Rev. Mexicana Astron. Astrofis., 49, 345
- Elmegreen, B. G., Lada, C. J., & Dickinson, D. F. 1979, ApJ, 230, 415
- Federrath, C., & Klessen, R. S. 2012, ApJ, 761, 156
- Federrath, C. 2015, MNRAS, 450, 4035
- Feng, Y., & Krumholz, M. R. 2014, Nature, 513, 523
- Field, G. B., Blackman, E. G., & Keto, E. R. 2011, MNRAS, 416, 710
- Fogerty, E., Frank, A., Heitsch, F., et al. 2016, MNRAS, 460, 2110
- Frau, P., Girart, J. M., Beltrán, M. T., et al. 2010, ApJ, 723, 1665
- Frau, P., Girart, J. M., Beltrán, M. T., et al. 2012, ApJ, 759, 3
- Frau, P., Girart, J. M., Alves, F. O., et al. 2015, A&A, 574, L6
- Galván-Madrid, R., Keto, E., Zhang, Q., et al. 2009, ApJ, 706, 1036
- Galván-Madrid, R., Vázquez-Semadeni, E., Kim, J., & Ballesteros-Paredes, J. 2007, ApJ, 670, 480
- Gavagnin, E., Bleuler, A., Rosdahl, J., et al. 2017, MNRAS, 472, 4155
- Girichidis, P., Konstandin, L., Whitworth, A. P., et al. 2014, ApJ, 781, 91
- Goodman, A. A., Rosolowsky, E. W., Borkin, M. A., et al. 2009, Nature, 457, 63
- Goldreich, P., & Kwan, J. 1974, ApJ, 189, 441
- González-Samaniego, A., & Vázquez-Semadeni, E. 2020, arXiv e-prints, arXiv:2003.12711
- Grudić, M. Y., Hopkins, P. F., et al. 2019, MNRAS, 488, 1501
- Hacar, A., Alves, J., Tafalla, M., & Goicoechea, J. R. 2017, A&A, 602, L2
- Hartmann, L., & Burkert, A. 2007, ApJ, 654, 988
- Heiner, J. S., Vázquez-Semadeni, E., & Ballesteros-Paredes, J. 2015, MNRAS, 452, 1353

- Heitsch, F., Hartmann, L. W., Slyz, A. D., Devriendt, J. E. G., & Burkert, A. 2008, *ApJ*, 674, 316
- Heyer, M., Krawczyk, C., Duval, J., & Jackson, J. M. 2009, *ApJ*, 699, 1092
- Ibáñez-Mejía, J. C., Mac Low, M.-M., Klessen, R. S., & Baczynski, C. 2016, *ApJ*, 824, 41
- Iffrig, O., & Hennebelle, P. 2015, *A&A*, 576, A95
- Jaffe, D. T., Guesten, R., & Downes, D. 1981, *ApJ*, 250, 621
- Jaffe, D. T., Stier, M. T., & Fazio, G. G. 1982, *ApJ*, 252, 601
- Jenkins, E. B. 2004, *Ap&SS*, 289, 215
- Jenkins, E. B., & Tripp, T. M. 2011, *ApJ*, 734, 65
- Kauffmann, J., Pillai, T., & Goldsmith, P. F. 2013, *ApJ*, 779, 185
- Kennicutt, R. C., Jr. 1998, *ApJ*, 498, 541
- Keto, E. R., & Myers, P. C. 1986, *ApJ*, 304, 466
- Kirk, H., Myers, P. C., Bourke, T. L., et al. 2013, *ApJ*, 766, 115
- Krumholz, M. R., & McKee, C. F. 2005, *ApJ*, 630, 250
- Lada, C. J., & Lada, E. A. 2003, *ARA&A*, 41, 57
- Lada, C. J., Lombardi, M., & Alves, J. F. 2010, *ApJ*, 724, 687
- Lada, C. J., Muench, A. A., Rathborne, J., Alves, J. F., & Lombardi, M. 2008, *ApJ*, 672, 410
- Larson, R. B. 1969, *MNRAS*, 145, 271
- Larson, R. B. 1981, *MNRAS*, 194, 809
- Lee, E. J., Miville-Deschênes, M.-A., & Murray, N. W. 2016, *ApJ*, 833, 229
- Leroy, A. K., Bolatto, A. D., Ostriker, E. C., et al. 2015, *ApJ*, 801, 25
- Lin, Y., Liu, H. B., Dale, J. E., et al. 2017, *ApJ*, 840, 22
- Liu, H. B., Galván-Madrid, R., Jiménez-Serra, I., et al. 2015, *ApJ*, 804, 37.
- Lombardi, M., Alves, J., & Lada, C. J. 2006, *A&A*, 454, 781
- Louvet, F., Neupane, S., Garay, G., et al. 2018, *arXiv:1810.12928*
- Mac Low, M.-M., & Klessen, R. S. 2004, *Reviews of Modern Physics*, 76, 125
- Mao, S. A., Ostriker, E. C., & Kim, C.-G. 2019, *arXiv e-prints*, *arXiv:1911.05078*
- Matzner, C. D., & McKee, C. F. 2000, *ApJ*, 545, 364
- McMullin, J. P., Waters, B., Schiebel, D., Young, W., & Golap, K. 2007, *Astronomical Data Analysis Software and Systems XVI*, 376, 127
- McKee, C. F. 1989, *ApJ*, 345, 782
- McKee, C. F., & Ostriker, J. P. 1977, *ApJ*, 218, 148
- McKee, C. F., & Ostriker, E. C. 2007, *ARA&A*, 45, 565
- McKee, C. F., & Williams, J. P. 1997, *ApJ*, 476, 144
- Muench, A. A., Lada, C. J., Rathborne, J. M., Alves, J. F., & Lombardi, M. 2007, *ApJ*, 671, 1820
- Naranjo-Romero, R., Vázquez-Semadeni, E., & Loughnane, R. M. 2015, *ApJ*, 814, 48
- Ohashi, S., Sanhueza, P., Chen, H.-R. V., et al. 2016, *ApJ*, 833, 209
- Oka, T., Hasegawa, T., Sato, F., et al. 2001, *ApJ*, 562, 348
- Onishi, T., Kawamura, A., Abe, R., et al. 1999, *PASJ*, 51, 871
- Padoan, P., Pan, L., Haugbølle, T., & Nordlund, Å. 2016, *ApJ*, 822, 11
- Peretto, N., Fuller, G. A., Duarte-Cabral, A., et al. 2013, *A&A*, 555, A112
- Peretto, N., Fuller, G. A., André, P., et al. 2014, *A&A*, 561, A83
- Peretto, N., Hennebelle, P., & André, P. 2007, *A&A*, 464, 983
- Peretto, N., & Fuller, G. A. 2009, *A&A*, 505, 405
- Pety, J. 2005, *SF2A-2005: Semaine De L'astrophysique Francaise*, 721
- Povich, M. S., & Whitney, B. A. 2010, *ApJL*, 714, L285
- Povich, M. S., Townsley, L. K., Robitaille, T. P., et al. 2016, *ApJ*, 825, 125
- Rathborne, J. M., Jackson, J. M., & Simon, R. 2006, *ApJ*, 641, 389
- Rathborne, J. M., Lada, C. J., Muench, A. A., Alves, J. F., & Lombardi, M. 2008, *ApJS*, 174, 396
- Roberts, W. W. 1969, *ApJ*, 158, 123
- Román-Zúñiga, C. G., Alves, J. F., Lada, C. J., & Lombardi, M. 2010, *ApJ*, 725, 2232
- Rosolowsky, E. W., Pineda, J. E., Kauffmann, J., & Goodman, A. A. 2008, *ApJ*, 679, 1338-1351
- Sánchez-Monge, Á., Palau, A., Fontani, F., et al. 2013, *MNRAS*, 432, 3288
- Sanhueza, P., Jackson, J. M., Zhang, Q., et al. 2017, *ApJ*, 841, 97
- Schmidt, M. 1959, *ApJ*, 129, 243
- Schneider, N., Csengeri, T., Bontemps, S., et al. 2010, *A&A*, 520, A49
- Shimoikura, T., Dobashi, K., Hirose, A., et al. 2019, *PASJ*, 82
- Solomon, P. M., Rivolo, A. R., Barrett, J., & Yahil, A. 1987, *ApJ*, 319, 730
- Springel, V. 2005, *MNRAS*, 364, 1105
- Traficante, A., Fuller, G. A., Smith, R., et al. 2015, *EAS Publications Series*, 75, 185
- Traficante, A., Fuller, G. A., Smith, R. J., et al. 2018a, *MNRAS*, 473, 4975
- Traficante, A., Lee, Y.-N., Hennebelle, P., et al. 2018b, *A&A*, 619, L7
- Vázquez-Semadeni, E., Ballesteros-Paredes, J., & Rodríguez, L. F. 1997, *ApJ*, 474, 292
- Vázquez-Semadeni, E., Gómez, G. C., Jappsen, A. K., et al. 2007, *ApJ*, 657, 870
- Vázquez-Semadeni, E., Gómez, G. C., Jappsen, A.-K., Ballesteros-Paredes, J., & Klessen, R. S. 2009, *ApJ*, 707, 1023
- Vázquez-Semadeni, E., González-Samaniego, A., & Colín, P. 2017, *MNRAS*, 467, 1313
- Vázquez-Semadeni, E., Zamora-Avilés, M., Galván-Madrid, R., & Forbrich, J. 2018, *MNRAS*, 479, 3254
- Vázquez-Semadeni, E., Palau, A., Ballesteros-Paredes, J., et al. 2019, *MNRAS*, 490, 3061
- Wang, P., Li, Z.-Y., Abel, T., et al. 2010, *ApJ*, 709, 27
- Xu, Y., Moscadelli, L., Reid, M. J., et al. 2011, *ApJ*, 733, 25
- Zamora-Avilés, M., Vázquez-Semadeni, E., & Colín, P. 2012, *ApJ*, 751, 77
- Zamora-Avilés, M., & Vázquez-Semadeni, E. 2014, *ApJ*, 793, 84
- Zuckerman, B., & Evans, N. J., II 1974, *ApJL*, 192, L149